Politechnika Wrocławska

Wydział Podstawowych Problemów Techniki

MASTER'S THESIS

Studies of electronic properties of atomically thin nanostructures with tight-binding model and DFT methods

Ludmiła Szulakowska

Supervisor:
Prof. dr hab. inż. Arkadiusz Wójs

Keywords: transition metal dichalcogenides, molybdenum disulphide, molybdenum diselenide, nanoribbons, nanostructures, tight-binding model, density functional theory, spin-polarisation, ferromagnetism,

Abstract: In this work we study theoretically various atomically-thin transition metal dichalcogenide (TMDC) nanostructures, including TMDC monolayers and nanoribbons (NRs). Their electronic and magnetic properties are investigated with three-band approximation to tight-binding (TB) model and within density functional theory (DFT) methods. Band structures with spin-splitting induced by spin-orbit coupling are analysed in TB model. In DFT calculations the edge spin-polarisation for narrow zigzag-edged MoS_2, MoSSe and $MoSe_2$ NRs is identified.

Table of contents

1 Introduction.

Since the discovery of graphene [1, 2] – one-atom-thin layer of hexagonally arranged carbon atoms – exploration of two-dimensional (2D) materials has begun, revealing unusual properties and numerous potential application prospects [3–6]. Regardless of unique nature of charge carriers in graphene [7, 8], its gapless electronic structure imposes limitations over its use in nanoelectronics and therefore sparks intensive interest in other materials with band gap in semiconducting regime [9, 10].

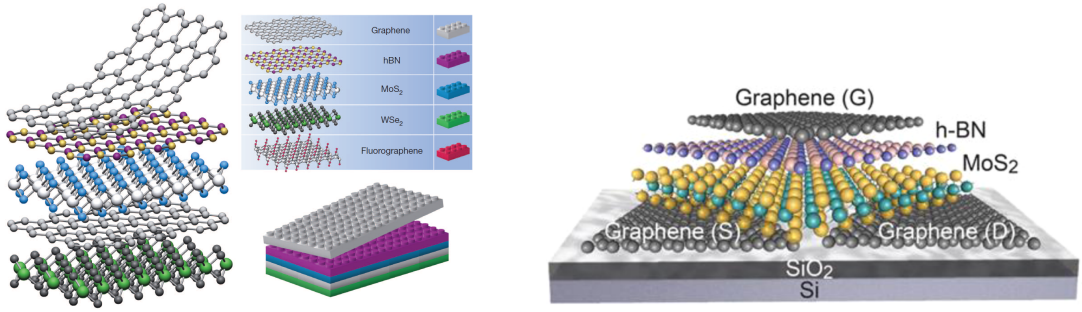

(a) **(b)**

Figure 1 – (a) Forming of the van der Waals heterostructure analogically to the Lego blocks. Large variety of heterotructures is possible. [11] (b) A field-effect transistor built of heterogenously stacked 2D materials. [12]

Among these there are various kinds of van der Waals (vdW) crystals like hexagonal boron nitride or 2D transition metal dichalcogenides, which have been intensively explored in the past decades for their diverse properties [13–15]. The nanostructures of vdW crystals have proved to be easily obtained and patterned through chemical and mechanical techniques [16–18]. Moreover, their separate layers can be stacked vertically due to weak vdW interactions between adjacent layers, which allows for forming of heterostructures with tailored properties (such heterostructures are shown in Fig. 1). Such materials make highly suitable ingredients for components of next-generation nanoelectronic devices, as well as give rise to new physical phenomena [19].

1.1 Crystals of transition metal dichalcogenides (TMDCs).

2D transition metal dichalcogenides (TMDCs) are a vast family of vdW crystals that can be exfoliated into monolayers showing distinct properties from bulk structures [9, 20–22]. These 2D materials can be regarded as semiconductor analogues of graphene, their lattice consisting of three strongly bonded planes of hexagonally packed atoms: X-M-X, where M atoms are molybdenum or tungsten and X atoms are selenium, sulphur or tellurium [1] (shown in Fig. 2a). Similarly to graphene, these trilayers, loosely coupled to each other by van der Waals interactions, have proven easy to exfoliate mechanically into 2D monocrystals [23]. On the other hand, the strong intra-planar bonding accounts for mechanical strength of the crystal. The characteristic stacking of M atom between two chalcogen planes saturates all ions, reducing the crystal's reactivity and enabling realisation of free-standing monolayers [24]. The arrangement of atoms may form ABA stacking with M atoms trigonal-prismatically coordinated with six X atoms in 2H structure or ABC stacking with M atoms octahedrally coordinated in the 1T structure (shown in Fig. 3A-B) [25].

It has been reported that these two similar structures, 2H and 1T of MX_2, show very different properties due to different stacking of atoms in monolayers. For molybdenum disulphide (MoS_2) the 2H crystal has been described as large-gap semiconductor [26] while the 1T structure is metallic and unstable, spontaneously distorting into 1T' crystal (shown in Fig. 3C) [27, 28].

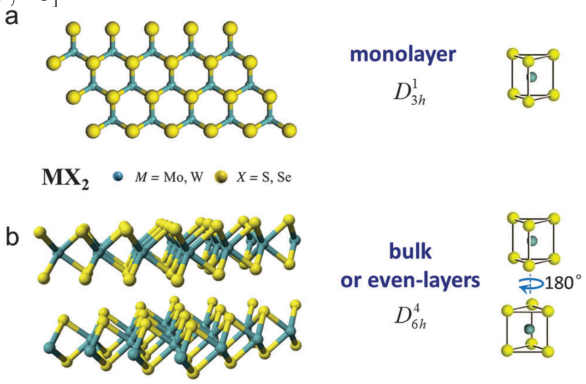

Figure 2 – Crystal structure of bulk and monolayer TMDCs shown schematically. (a) Top view of a monolayer TMDC and the unit cell which shows the inversion symmetry breaking. (b) Even-layered TMDC crystal and its unit cell with the inversion center in between the planes. [29]

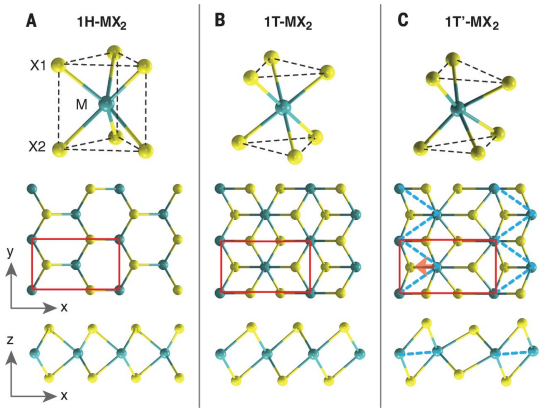

Figure 3 – Different coordination of metal atoms in TMDCs: 2H (A), 1T (B), 1T' (C) [29]

Monolayers of TMDCs have been already successfully synthesized with the use of techniques like liquid exfoliation (shown in Fig. 5) [23] or micromechanical cleavage [9,30]. Planes of $MoSe_2$ and MoS_2 have also been obtained with selenisation and sulphurisation of MoO_3 via chemical vapour deposition on various substrates (schematically shown in Fig. 4) [31, 32].

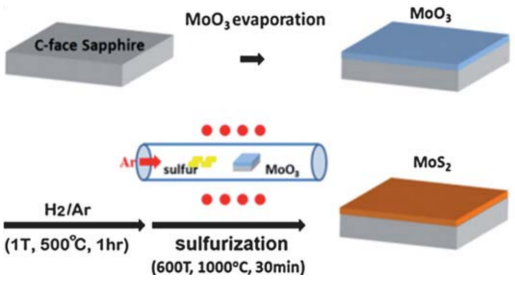

Figure 4 – Schematic illustration of the sulphurisation method. MoO_3 is evaporated on sapphire substrate and then is converted to MoS_2 in a two-step thermal process. [32]

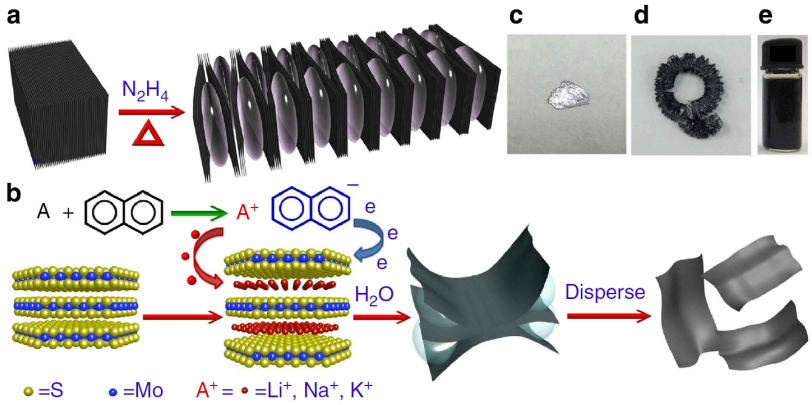

Figure 5 – (a) Bulk MoS_2 is pre-exfoliated by the decomposition products of N_2H_4. (b) Sample is intercalated and disperses into monolayers in water. (c) Photograph of bulk MoS_2. (d) Photograph of pre-exfoliated MoS_2. (e) Photograph of MoS_2 dispersion in water. [23]

1.2 Electronic properties of TMDCs.

2D TMDCs have become promising materials to complement the shortcomings of graphene, which despite its high carrier mobilitties is semimetallic [2]. Thus, in search of practical application TMDCs have started to play bigger role due to their appreciable band gaps and structural similarity to graphene.

Among TMDCs monolayer of MoS_2 has been most widely studied and recent reports on properties of $MoSe_2$ have also been presented [33]. These are intrinsic semiconductors with direct band gap in the visible frequency range (∼1.8 eV for MoS_2 and 1.5 eV for $MoSe_2$) [33–35], what makes them most favourable for optoelectronic devices. A transition from indirect band gap in bulk several TMDC materials to direct band gap for monolayer has also been reported (this is shown in Fig. 6) [33, 35]. Whereas in graphene and bulk MoS_2 high carrier mobilities have been observed [5, 36], single layer of MoS2 is found to have low mobility due to substrate used in experiments [1,3]. It has been argued that both substrates and contacts influence the performance of devices built with MoS_2 [37, 38].

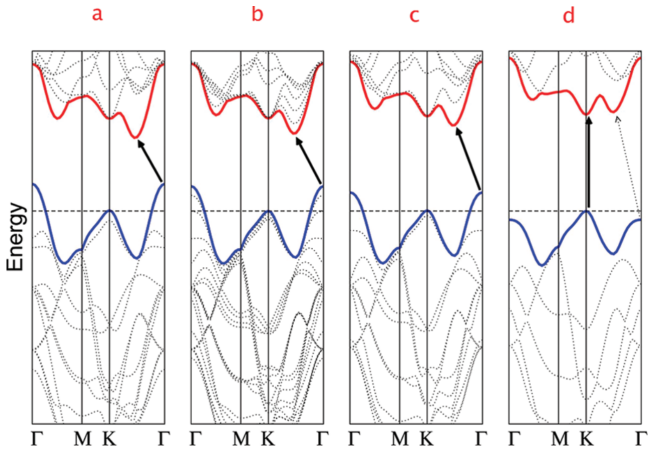

Figure 6 – Transition from bulk MoS_2 band structure (a) with an indirect band gap to band structures of thinner crystals (b,c) and to a monolayer (d) with a direct band gap. [22]

Analogically to graphene, for TMDCs monolayers valence and conduction band edges are located in two inequivalent valleys K and K' in the corners of hexagonal Brillouin

zone (BZ) (shown in Fig. 7) [39]. This gives the charge carriers an extra discrete degree of freedom, which may be used to encode and process information [40–42]. Moreover, there is whole new range of phenomena related to electron's spin in TMDCs because of large spin-orbit coupling (SOC) induced by d orbitals of heavy metal atoms, which creates substantial spin splitting of valence band and smaller – of conduction band for these materials [43].

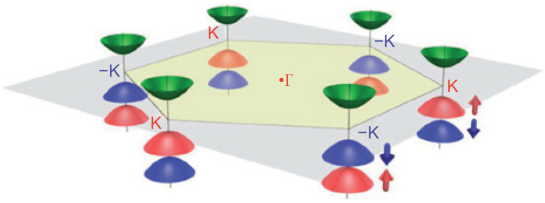

Figure 7 – Schematic illustration of the MoS_2 band structure at band edges located in the K and K' valleys of a hexagonal Brillouin zone. Large spin-splitting of the valence band is visible and the spin bands are reversed for K and K' points. [19]

Notably, the inverse-symmetry breaking in 2H-coordinated TMDCs monolayers (illustrated in Fig. 2a as opposed to Fig. 2b), together with strong SOC, induces valley-dependent optical transition selection rules which allow for distinction of these valleys. This is due to interband transitions in K and K' valleys, which couple to left- and right-circularly polarised light (shown in Fig. 8) [19, 44] . First experimental demonstrations of valley polarization by pumping with circularly polarised beams have been reported for MoS_2 and WS_2 [44–47].

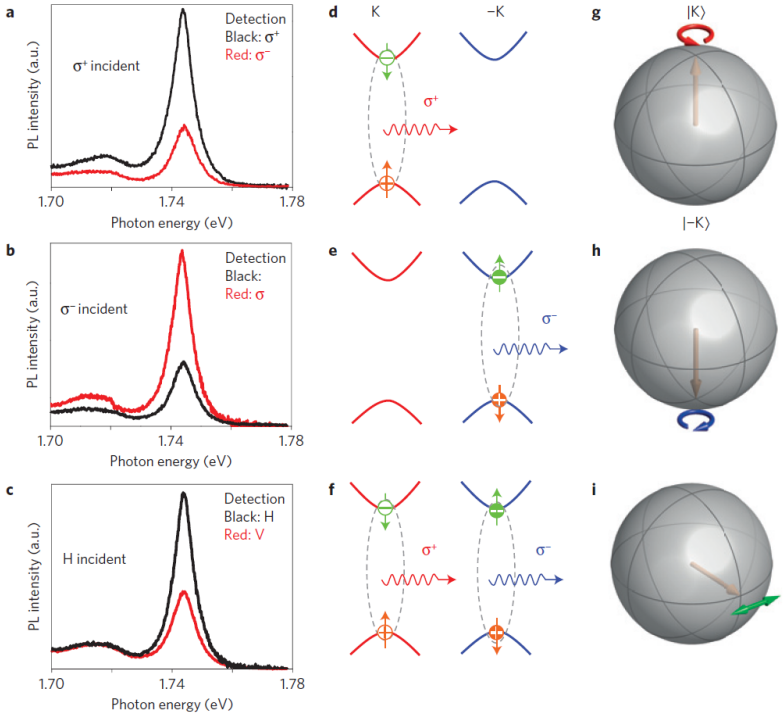

Figure 8 – Demostration of optical control of the valley polarisation for monolayer TMDCs. (a-c) Polarisation-resolved photoluminescence of excitons in WSe_2 by (a) left, (b) right and (c) linearly polarised light. (d-f) Band structure edges diagrams with polarised emission corrsponding to a-c respectively. (g-i) Polarised excitations represented on the Bloch sphere corresponding to a-c respectively. Arrows outside of the Bloch sphere show light polarisation and the arrows inside it - valley pseudospin. [48]

In view of these results, there exists a strong coupling of spin to valley degree of freedom for TMDC materials. Importantly, the valley-contrasting spin splitting implies that the spin-split alone processes are forbidden [19]. This occurs as the time-reversal symmetry requires that the bands in opposite valleys are of opposite spin-splitting (shown in the schematic drawing in Fig. 7), which means that the valley carriers can be also distinguished by their spin moments. In addition, large separation of valleys in momentum space allows for long spin coherence times as the intervalley scattering is suppressed [49, 50]. Such fundamental properties of TMDCs suggest that these materials may be effectively used for spintronics and valleytronics.

1.3 Physical phenomena in TMDCs.

These materials are also a particularly interesting platform for research due to phenomena absent in graphene because of its weak spin-orbit coupling and conservation of inverse-symmetry. Firstly, new properties of TMDCs may be observed when external electric field is applied. In such case carriers of different spin and valley index (called pseudospin [49]) tend to flow in the opposite directions and accumulate on transverse boundaries of the sample, causing spin and valley polarisation. These are spin and valley Hall effects (shown in Fig. 9) [19, 49]. It has been reported that photoinduced spin Hall and valley Hall effects are responsible for long lived polarisations both in electron-doped and hole-doped systems [19]. This introduces an efficient way of electrical manipulation of optically generated excitonic states [49].

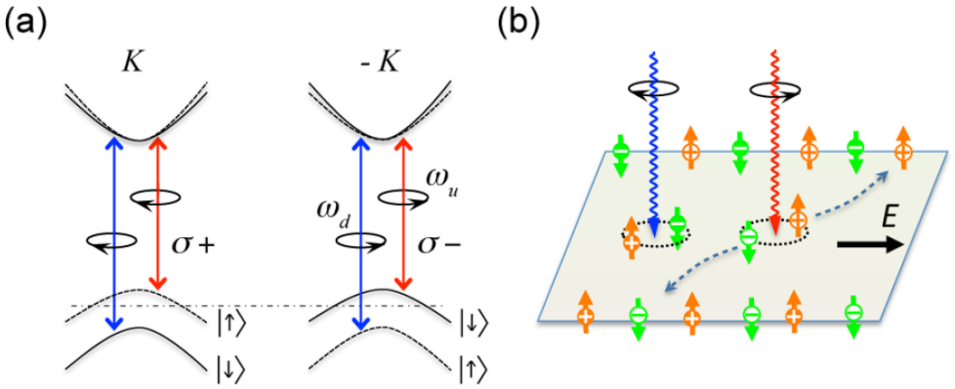

Figure 9 – Coupled spin and valley physics in monolayer TMDCs. (a) Valley and spin optical transition selection rules. Spin-split bands with the corresponding spins are shown. ω_u (red) and ω_d (blue) are transition frequencies from the spin-split valence band tops to the conduction band bottom. Carriers in opposite valleys are excited by the light of opposite polarisations. (b) Spin and valley Hall effects of electrons and holes excited by (in K) right- and (in -K) left-polarised light of two diffeent frequencies ω_u and ω_d (like in a.). The carriers are dissociated by an in-plane electric field and move to the two opposite boundaries of the sample, creating Hall current. Electrons and holes from the two opposite valleys are marked by '-' and '+' symbols, respectively, with the colors inverted for opposite valleys. [19]

Secondly, TMDCs 2D crystals exhibit peculiar magnetic-induced properties, highly distinguishable from graphene. It has been reported that magnetic field provides simple method of controlling valley and spin polarisation in 2D TMDCs [49]. In external magnetic field Landau levels (LL) are non-uniformly spaced and the zeroth LL is shifted in opposite directions for the two valleys (illustrated by Fig. 10a). This asymmetric behaviour can be explained in terms of Zeeman effect for pseudospin which produces an additional orbital

magnetic moment [49]. In magnetic field the energy bands are thus shifted accordingly to valley-contrasting magnetic moments [49, 51]. This effect lifts the valley degeneracy and has been referred to as the pseudospin-orbit coupling [49, 52].

As an effect of this, the zeroth LL is located at the top of valence band in K valley and at the bottom of conduction band in K' valley (shown in Fig. 10b). Interestingly, due to spin splitting of the valence bands low doping results in 100% spin polarisation of a single valley, which can be inverted with reversed field. Larger doping leads to occupation of higher LL and depolarisation. This allows the valley polarization to be controlled by tuning the external magnetic field and the doping level [49]. Moreover, this shows that the polarization selection rules for the inter-LL transitions are valley dependent and therefore circularly polarized light may excite carriers in separate valleys, coupling photon handedness to the exciton valley degree of freedom [53, 54].

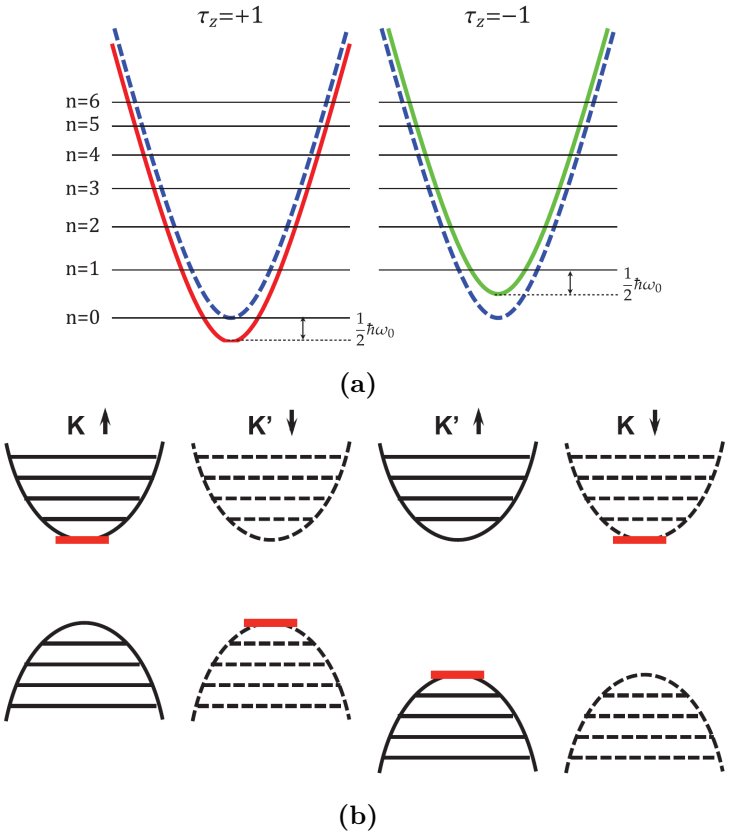

Figure 10 – Magnetic control of the valley degree of freedom in TMDCs. (a) The assymetric LL structure for the conduction band of the two valleys (in solid black lines). The 0th LL is located $\hbar\omega/2$ above the bootim of the conduction band. The red and green solid curves show the band dispersion in opposite valleys shifted due to the pseudo-spin orbit coupling (see text for explanation). Dashed lines show the original band dispersion without the magentic field. (b) LLs for carriers in TMDCs. Solid (dashed) lines stand for spin-up (-down) bands and the horizontal lines show the LL structure. The four red dashes show the location of the 0th LL for each spin and valley. [49]

Furthermore, a topological insulating phase has been recently reported in atomic crystals of TMDCs [55]. It emerges due to structural distortions of the 1T-coordinated lattice of WSe2 and other TMDCs (it is named 1T' structure [55]), which cause intrinsic band inversion of chalcogenide-p and metal-d bands [55]. Such band structure is here connected to properties characterisitc for QSH insulators. This includes insulating bulk and

existence of conducting edge states (their electronic structure shown in Fig. 11), which are topologically protected from backscattering by time reversal symmetry. Additional benefits from utilisation of these materials as topological insulators are a large inverted band gap (over 0.6 eV [55]) in comparison to other crystals with such properties as well as possibility of tuning it with both in-plane elastic strain and external electric field [55]. These findings bring prospects for successful operation of novelty quantum electronic devices. In addition to these numerous effects apparent in TMDC crystals, there have been reports of discovery of a superconducting phase in thin films of MoS_2 [24, 56], making it an interesting material for both fundamental research and application-oriented studies.

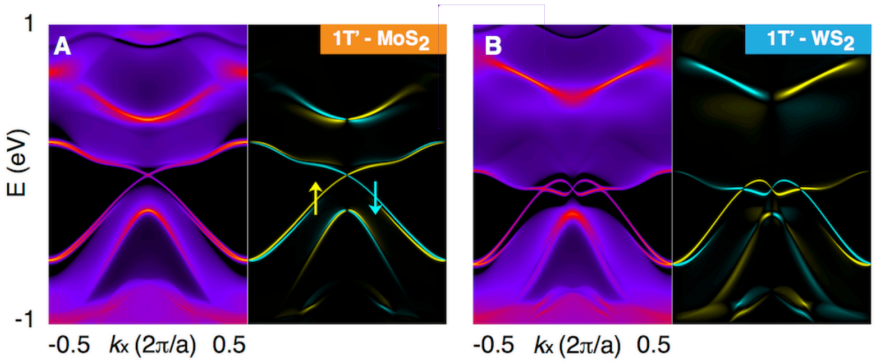

Figure 11 – Edge states electronic structure of topologically insulating TMDC crystals. (a-b) Left panel shows the density of states and the right panel - spin-polarisation. [55]

1.4 TMDC nanostructures.

With all the possible application prospects of TMDCs in nanoelectronics taken into account it is vital to investigate the properties of nanostructures of these materials. It has been expected that they differ significantly from these of bulk materials due to confinement effect, edge contribution, chemical reactivity and particle interactions. Naturally, many degrees of freedom for monolayer TMDCs suggest the usage of single electron as an information carrier for spintronic and valleytronic devices [57]. Since the desired properties of bulk materials involve carrier's valley index processes, it has been of huge importance to determine whether valley physics is preserved in nanostructured TMDCs. Interestingly, recent results have shown that the valley hybridization is negligible in TMDC quantum dots (QDs) and therefore pseudospin is then a valid degree of freedom. [57]. This observation motivates intensive application-oriented exploration of phenomena present in TMDC nanostructures.

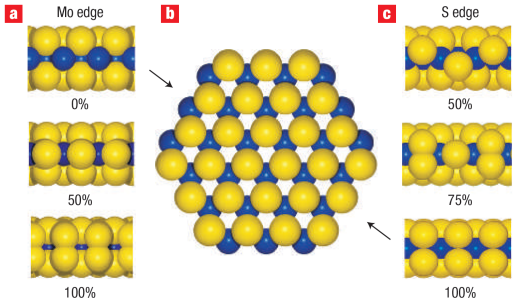

Figure 12 – (b) A MoS_2 nanocluster with two edge types (a,c) and sulphur coverage percentages. Blue balls are Mo atoms and yellow - sulphur atoms. [58]

An additional motivation for theoretical studies of such structures are numerous experimental cases of TMDCs obtained in nanoscale [59–64] and reports on devices operating on their basis [65–69]. MX_2 nanocrystals with various sizes, edge types or terminations have been obtained and favourable shapes for specific compounds have been determined. Several edge types possible for MoS_2 nanoclusters are shown in Fig. 13. Also, experimental results have shown that triangular shapes are most frequently observed for S-passivated QD edges due to sulphur excess [70]. Additionally, synthesis of TMDC fullerene-like structures, nanowires and nanotubes has been reported [71–73]. Recently, extremely narrow MoS2 nanoribbons have also been obtained heating of carbon nanotubes in presence of molybdenum compounds [74].

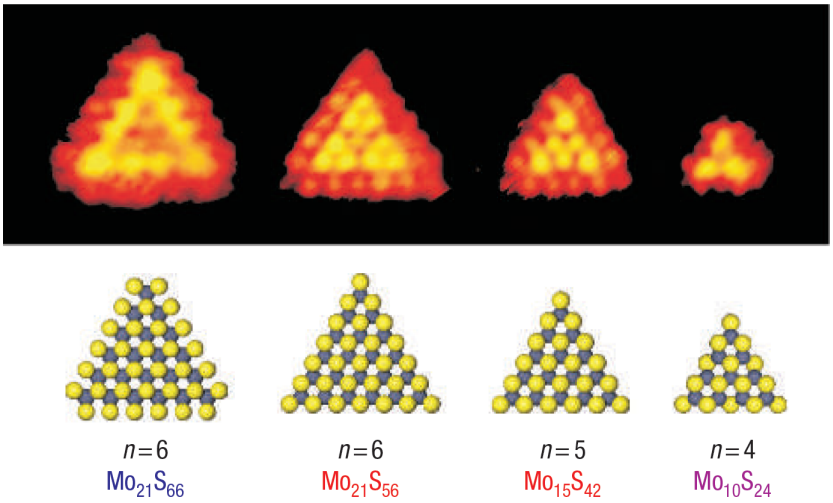

Figure 13 – Experimentally observed triangular MoS_2 quantum dots. This shape is favoured in case of MoS_2. First quantum dot from the left is Mo-edged with S-passivation and the remaining 3 structures are of S-edge. [58]

In view of this, various TMDCs nanostructures have been widely studied in order to determine their diverse properties. Reports on density functional theory (DFT) geometry optimisation of MoS_2 QDs have been presented [70, 75, 76] as well as electronic and magnetic properties of MoS_2 nanoribbons (NRs) have been analysed [77, 78]. Also, recently a few simple tight-binding (TB) models have been proposed to describe low-energy electronic structure of planar TMDC crystals and NRs [39, 79–82].

Among various nanostructured TMDCs nanoribbons might prove highly useful for nanoelectronic applications. This has encouraged intensive research in this area, mainly for the widely-explored MoS_2. It has been predicted that the TMDC monolayers might be easily tailored into NRs with zigzag and armchair edge types of different passivations and atom termination. Stability, electronic and magnetic properties of various sizes and edge types of NRs have been already analysed theoretically [77, 83–91].

Contrary to the bulk properties of MoS_2, recent studies have identified zigzag-edged MoS_2 NRs (MoS2 ZNRs) as metallic [89, 90, 92, 93], whereas armchair-edged MoS_2 NRs (MoS_2 ANRs) have been reported to show semiconducting properties [89, 90, 92–94]. This has proven true in many passivation types of the metal atom edges [95] and is observed also for WS_2 ANRs. Passivation with carbon and hydrogen atoms has also been reported to increase the band gap of the MoS_2 ANRs [95]. Layered NRs have also been studied [89].

Interestingly, TMDC NRs exhibit magnetic behaviour which can be influenced by numerous factors. Most of these unusual properties stem from the magnetic moments

placed at the edge atoms, especially for metal-dominated edges [78]. MoS_2 ZNRs have been shown to be ferromagnetic (shown in Fig. 14a) [89, 90]. The ANRs on the other hand exhibit no magnetism [89]. Although weaker, the ferromagnetism remains for hydrogenated MoS_2 [90], while WS_2 ZNRs have been identified as antiferromagnetic (shown in Fig. 14b) [78]. Magnetic properties of MoS_2 zigzag edges in nanocrystals have been studied experimentally as well [96, 97].

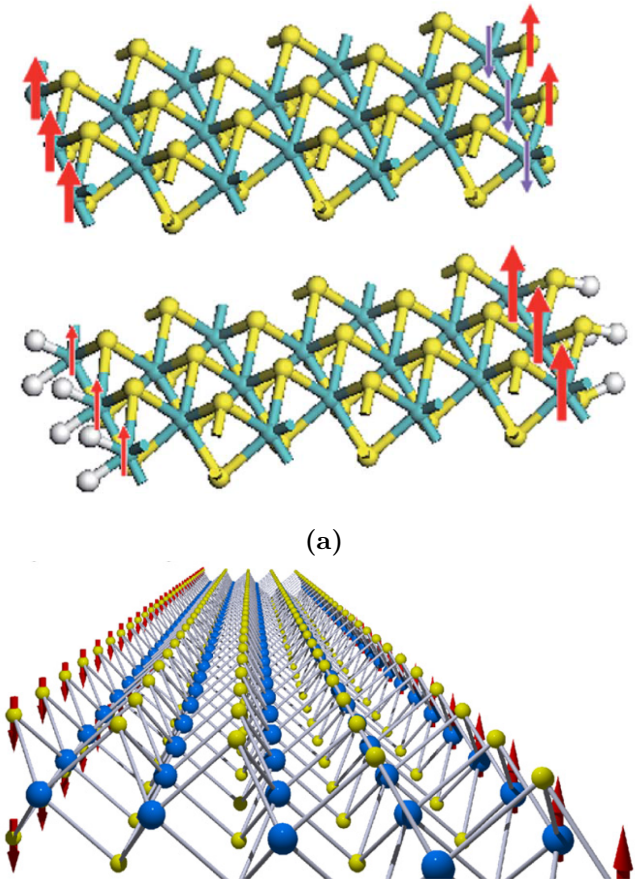

(a)

(b)

Figure 14 – (a) Spin-polarisation of edges of a MoS_2 nanoribbon (top) unpassivated and (bottom) hydrogen-passivated. For unpassivated case the alignment of spin is ferromagentic ($\uparrow\uparrow$) and remains so after hydrogen-passivation, though weaker. Thicker arrows show larger magnetisation and the colors are for opposite spins. [77] (b) Anti-ferromagnetic ($\uparrow\downarrow$) spin polarisation for a WS_2 nanoribbon. [78]

Importantly, in case of sulphur-termination the magnetism of MoS_2 ZNRs depends strongly on the coverage percentage of the sulphur atom on the edges and changes drastically if edge defects or vacancies are introduced [98, 99]. This demonstrates how sensitive these structures are to the edge characteristics. Another important conclusion from these results regards the equally strong contribution of Mo-edge and S-edge to the magnetization.

Other means of influencing the magnetic and electronic properties of TMDCs nanoribbons include external fields [83, 100] and applied strain [87, 91, 92, 101] (MoS_2 NRs have proved to be stretchable up to a strain of 10%). As the magnetic moment of strained NRs is increased [87], it has been predicted that applying strain may be used to control the band gap and engineer their magnetic moment.

In addition to all the means of streering the nanoribbons properties, an effective method of obtaining devices with tailored characteristics is combining the TMDC nanocrystals into in-plane heterostructures. This is especially desirable in case of TMDCs with close-matched lattice constants as this reduces strain and inhomogeneities on the interfaces. For TMDCs of very similar lattice constants the mismatch may be even an order of magnitude smaller than for graphene and hexagonal boron nitride [63]. Such heterostructure of very sharp interfaces have been already observed experimentally for MoS_2-WS_2 and $MoSe_2$-WSe_2 nanocrystals (shown in Fig. 15) [63, 64] and studied theoretically [102].

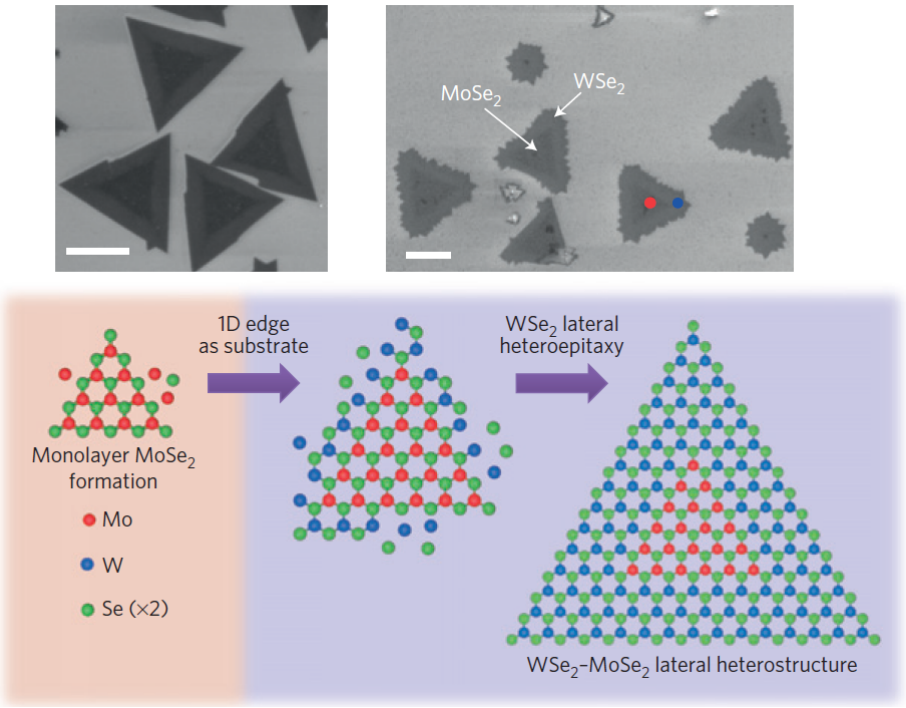

Figure 15 – In-plane heterostructures of $MoSe_2$ and WSe_2 nanocrystals. (top) Scanning tunneling microscopy (SEM) images of heterostructure crystals from two different growths. Both scale bars indicate a $10\mu m$ distance. (bottom) Schematic illustration of the in-plane heteroepitaxy process. [63]

The research done in pursue of better understanding of unusual properties of TMDC materials brought discovery of numerous effects and detailed description of a high diversity of nanostructures [60, 70, 77, 87]. Many of these results indicate that these crystals give promising perspectives to the next-generation nanoelectronics, spintronics and valleytronics. Yet, still this research area encourages unceasingly wide exploration of TMDC crytstals' properties and establishes strong motivation for further studies in this matter.

2 Methodology.

In this chapter the methodology of this work is explained. Section 2.1 provides description of tight-binding theory, which was the base for performed calculations. Later, an overview of density functional theory is presented, together with the details of the computations in the Abinit package.

2.1 Tight-binding model.

Tight-binding model has proved a valuable tool used to determine the electronic properties of many 2D materials and has been used for calculating the band structures of TMDC materials [39,79]. Here, the tight-binding theory is explained [103] and the details of the three-band approximation are presented.

2.1.1 General description.

Tight-binding (TB) model assumes that the crystal potential is strong and it bounds electrons to the atoms in result. This means that the electrons are captured by ions during their motion through lattice and do not interact noticeably with other far-away atoms. Therefore, their wavefunctions may be constructed as a linear combination of the atomic orbitals, which represents the *linear combination of atomic orbitals (LCAO)* approximation. The main assumption of the model is that these orbitals are modified only slightly by other atoms in the solid and this modification may be viewed as a small perturbation.

Let us consider electrons in a solid, where atomic orbitals of a free atom are affected by the presence of other atoms. Because of a translational symmetry of a crystal lattice, its wavefunction must be an eigenstate of a translation operator:

$$\hat{T}_{\boldsymbol{R}}\psi^{\boldsymbol{k}}(\boldsymbol{r}) = \psi^{\boldsymbol{k}}(\boldsymbol{r}+\boldsymbol{R}), \tag{2.1}$$

where $\boldsymbol{k}$ is wave vector and $\boldsymbol{R}$ is a vector of translation operation. Also, from the Bloch's theorem, wavefunctions of electrons in periodic system are Bloch waves:

$$\psi^{\boldsymbol{k}}(\boldsymbol{r}-\boldsymbol{R}) = e^{i\boldsymbol{k}\boldsymbol{R}}u(\boldsymbol{r}) \tag{2.2}$$

and form a basis of eigenstates of the Hamiltonian. In the expression above $u(\boldsymbol{r})$ has the periodicity of the lattice. We may therefore express the wavefunction of our system as follows:

$$\psi^{\boldsymbol{k}}(\boldsymbol{r}) = \frac{1}{\sqrt{N}}\sum_{\boldsymbol{R},\alpha} e^{i\boldsymbol{k}\boldsymbol{R}}\phi_\alpha(\boldsymbol{r}-\boldsymbol{R}) = \frac{1}{\sqrt{N}}e^{i\boldsymbol{k}\boldsymbol{r}}\sum_{\boldsymbol{R},\alpha} e^{-i\boldsymbol{k}(\boldsymbol{r}-\boldsymbol{R})}\phi_\alpha(\boldsymbol{r}-\boldsymbol{R}) \tag{2.3}$$

where $\phi(\boldsymbol{r}-\boldsymbol{R})$ are atomic orbitals localised on an atom in the cell located at $\boldsymbol{R}$ and the wave function has a Bloch form. We may determine the electron energy:

$$
\begin{aligned}
E(k) &= \langle\psi_k|\,\hat{H}\,|\psi_k\rangle \\
&= \frac{1}{N}\sum_{\boldsymbol{R},\boldsymbol{R'},\alpha,\beta} e^{i\boldsymbol{k}(\boldsymbol{R}-\boldsymbol{R'})}\,\langle\phi_\alpha(\boldsymbol{r}-\boldsymbol{R'})|\,\hat{H}\,|\phi_\beta(\boldsymbol{r}-\boldsymbol{R})\rangle \\
&= \langle\phi(\boldsymbol{r})|\,\hat{H}\,|\phi(\boldsymbol{r})\rangle + \sum_{\boldsymbol{R},\alpha,\beta}{}' e^{i\boldsymbol{k}\boldsymbol{R}}\,\langle\phi_\alpha(\boldsymbol{r})|\,\hat{H}\,|\phi_\beta(\boldsymbol{r}-\boldsymbol{R})\rangle\,,
\end{aligned}
\tag{2.4}
$$

where $\sum'_{\boldsymbol{R},\alpha,\beta}$ means summing over all lattice sites at $\boldsymbol{R}\neq\boldsymbol{0}$, α,β are the orbital indices and

$$
\hat{H} = \hat{E}_{kin} + \hat{V}. \tag{2.5}
$$

The first term in (2.4) corresponds to electron's onsite energy. The second term of this expression describes effects of an electron tunnelling to other atoms in the lattice. Sometimes the nearest-neighbour approximation is taken, which neglects the contributions from atoms farther than the nearest-neighbours.

Let us examine the second term in (2.4) in the nearest-neighbour approximation:

$$
\begin{aligned}
&\sum_{\boldsymbol{R},\alpha,\beta}{}' e^{i\boldsymbol{k}\boldsymbol{R}}\,\langle\phi_\alpha(\boldsymbol{r})|\,\hat{H}\,|\phi_\beta(\boldsymbol{r}-\boldsymbol{R})\rangle = \\
&\quad= \sum_{\alpha,\beta}{}' \langle\psi_{\boldsymbol{k},\alpha}(\boldsymbol{r})|\,\hat{E_{kin}}\,|\psi_{\boldsymbol{k},\beta}(\boldsymbol{r}-\boldsymbol{r}_a)\rangle + \sum_{\alpha,\beta}{}' \langle\psi_{\boldsymbol{k},\alpha}(\boldsymbol{r})|\,\hat{V(\boldsymbol{r})}\,|\psi_{\boldsymbol{k},\beta}(\boldsymbol{r}-\boldsymbol{r}_a)\rangle \\
&\quad= e_{\boldsymbol{k}}\sum_{\alpha,\beta}{}' \langle\psi_{\boldsymbol{k},\alpha}(\boldsymbol{r})|\psi_{\boldsymbol{k},\beta}(\boldsymbol{r}-\boldsymbol{r}_a)\rangle + \sum_{\alpha,\beta}{}' \langle\psi_{\boldsymbol{k},\alpha}(\boldsymbol{r})|\,\hat{V(\boldsymbol{r})}\,|\psi_{\boldsymbol{k},\beta}(\boldsymbol{r}-\boldsymbol{r}_a)\rangle
\end{aligned}
\quad , \tag{2.6}
$$

where $\boldsymbol{r}_a$ is the lattice vector. The first term of the expression in (2.6) depends on the orbitals overlap and for orthogonal orbitals

$$
\langle\psi_{\boldsymbol{k},\alpha}(\boldsymbol{r})|\psi_{\boldsymbol{k},\beta}(\boldsymbol{r}-\boldsymbol{r}_a)\rangle = \begin{cases} 1 & \text{if } \alpha=\beta \\ 0 & \text{if } \alpha\neq\beta. \end{cases} \tag{2.7}
$$

The second term of the expression in (2.6) is the *hopping integral*, which determines the probability of an electron tunnelling to other atoms.

In a second quantisation form the Hamiltonian reads:

$$
\hat{H} = \sum_{i,\alpha}\epsilon_{i\alpha}\hat{c}^\dagger_{i\alpha}\hat{c}_{i\alpha} + \sum_{<i,j>,\alpha,\beta} t_{ij\alpha\beta}\hat{c}^\dagger_{i\alpha}\hat{c}_{j\beta}, \tag{2.8}
$$

where t_{ij} is the hopping integral and often we can simplify: $t_{ij\alpha\beta}=t_{\alpha\beta}$ for all tunneling processes between atomic sites i and j, $\epsilon_{i\alpha}$ is an onsite energy for orbital α and atomic site denoted by i and $\hat{c}^\dagger_i(\hat{c}_j)$ is a creation (annihilation) operator at the atomic site $i(j)$.

2.1.2 Three-band approximation.

Three-band approximation to the tight-binding model assumes that the calculations are performed in the basis of only three atomic orbitals

$$|\phi_1\rangle = d_{z^2},\ |\phi_2\rangle = d_{xy},\ |\phi_3\rangle = d_{x^2-y^2}. \tag{2.9}$$

of the metal atom in TMDC structures. The wavefunction of the system is then a linear combination of these atomic orbitals:

$$|\Psi_{\boldsymbol{k}}(\boldsymbol{r})\rangle = \sum_{\boldsymbol{R}} e^{i\boldsymbol{k}\boldsymbol{R}} |\Phi(\boldsymbol{r}-\boldsymbol{R})\rangle\,, \tag{2.10}$$

where

$$|\Phi(\boldsymbol{r})\rangle = \sum_{i=1}^{3} c_i\, |\phi_i(\boldsymbol{r})\rangle\,. \tag{2.11}$$

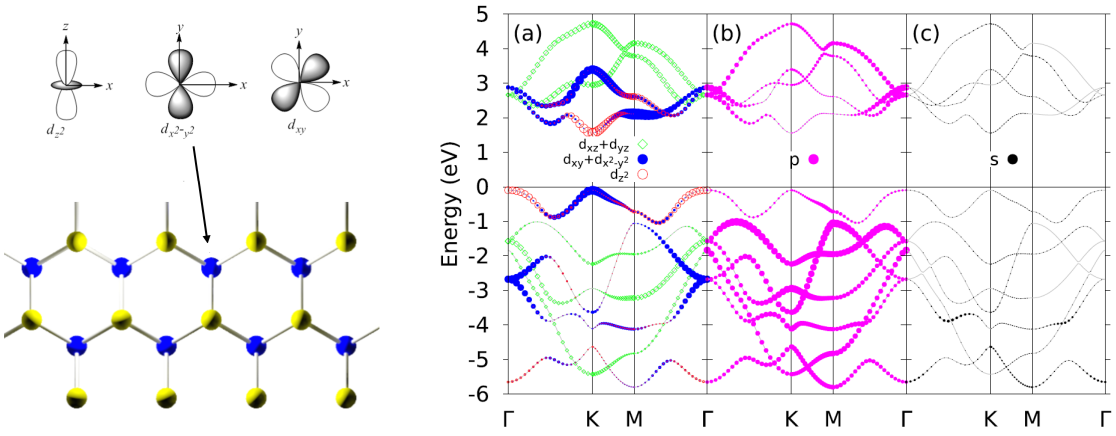

(a) **(b)**

Figure 16 – (a) The basis of the three-band approximation of tight-binding model for TMDC nanocrystals, consisting of three **d** metal orbitals given in (2.9). (b) The band structure of MoS_2 with the contribution of certain orbitals for each band marked with the variable-size and -color circles. The three **d** orbitals yield the most significant contribution to the low energy band structure. [39]

This is a reasonable assumption since the Bloch states near the band edges for monolayer MoS_2 and other TMDCs mostly consist of Mo d orbitals, especially d_{z^2}, d_{xy} and $d_{x^2-y^2}$ (shown in Fig. 16a), therefore we neglect the contribution from other d orbitals, p and s orbitals. We perform calculations of band structure of MoS_2 and other TMDC nanostructures considering only the nearest-neighbours (NN) **d-d** hoppings and express the Hamiltonian of the system in the three-band basis given by (2.9) (shown in Fig. 16b).

We calculate the matrix elements of our Hamiltonian as hopping integrals expressed in the second term of (2.6). The value of the integral depends on the type of orbital and on their relative position, i.e. their mutual distance as well as the angle of rotaion of an orbital in the frame of the other (this is shown in 17). Due to this, all such integrals can be expressed as a linear combination of three atomic bonds for orbitals in their unrotated position where the coefficients are determined by the *direction cosines* [104].

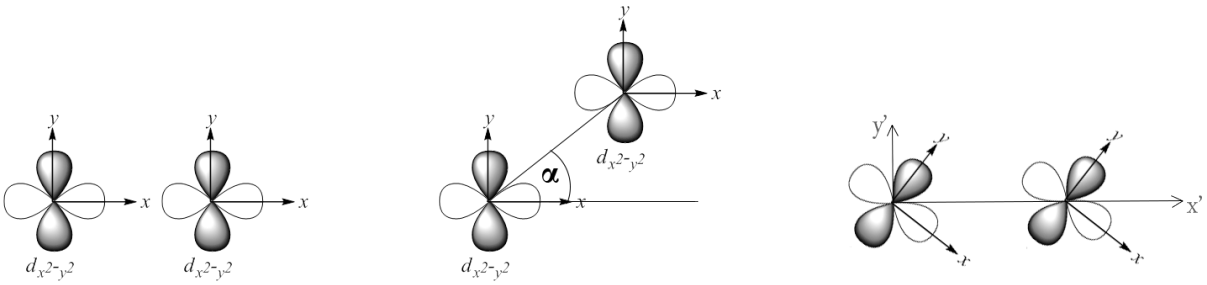

(a)

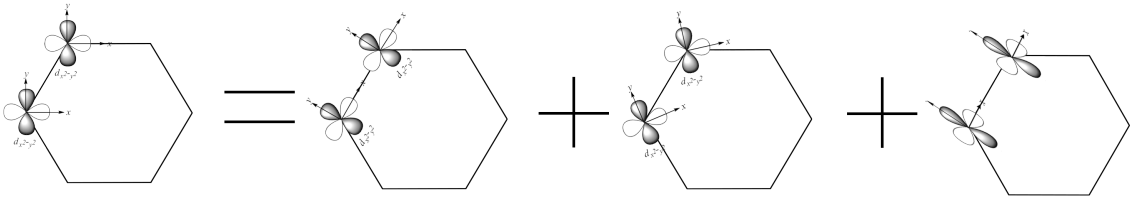

(b)

$E_{yz,\,3z^2-r^2}$	$\sqrt{3}mn\left[n^2-\frac{1}{2}(l^2+m^2)\right](dd\sigma)+\sqrt{3}mn(l^2+m^2-n^2)(dd\pi)-\frac{1}{2}\sqrt{3}mn(l^2+m^2)(dd\delta)$
$E_{zx,\,3z^2-r^2}$	$\sqrt{3}ln\left[n^2-\frac{1}{2}(l^2+m^2)\right](dd\sigma)+\sqrt{3}ln(l^2+m^2-n^2)(dd\pi)-\frac{1}{2}\sqrt{3}ln(l^2+m^2)(dd\delta)$
$E_{x^2-y^2,\,x^2-y^2}$	$\frac{3}{4}(l^2-m^2)^2(dd\sigma)+\left[l^2+m^2-(l^2-m^2)^2\right](dd\pi)+\left[n^2+\frac{1}{4}(l^2-m^2)^2\right](dd\delta)$
$E_{x^2-y^2,\,3z^2-r^2}$	$\frac{1}{2}\sqrt{3}(l^2-m^2)\left[n^2-\frac{1}{2}(l^2+m^2)\right](dd\sigma)+\sqrt{3}n^2(m^2-l^2)(dd\pi)+\frac{1}{4}\sqrt{3}(1+n^2)(l^2-m^2)(dd\delta)$
$E_{3z^2-r^2,\,3z^2-r^2}$	$\left[n^2-\frac{1}{2}(l^2+m^2)\right]^2(dd\sigma)+3n^2(l^2+m^2)(dd\pi)+\frac{3}{4}(l^2+m^2)^2(dd\delta)$

(c)

Figure 17 – Determining the hopping integrals of d metal orbitals. (a) Intuitive picture for determining the **d-d** orbital hopping integral: the integral between two orbitals $d_{x^2-y^2}$ at rotated crystal sites (middle) are distinguishable from the integral of orbitals at unrotated positions (left). It can viewed as rotating the orbitals themselves (right), which gives in this case a bond between the orbitals d_{xy} and thus, produces a different integral. (b) Every hopping integral of d-d orbitals may be expressed as a linear combination of hopping integrals of the three d-d bonds: σ, π, δ (ingredients of the sum from left to right). (c) Citation after J.C.Slater: the highlighted line states the $d_{x^2-y^2} - d_{x^2-y^2}$ hopping integral and is expressed with the use of the *direction cosines*. [104]

2.2 Density functional theory.

In this section the background for density functional theory calculations is described in detail. The theoretical approach is first presented [105] and it is followed by the computational aspects of the calculations performed.

2.2.1 Overview of the method.

When dealing with solids we must consider a system of heavy, positively charged nuclei and lighter, negatively charged electrons. In order to desribe the system's properties we need to solve a quantum many-body problem of $N_N + N_e$ interacting particles, where $N_{N(e)}$ is the number of nuclei (electrons). The Hamiltonian for the system reads:

$$\hat{H} = \Big(\sum_i^{N_N} \big(-\frac{\hbar^2}{2M_i} \nabla^2_{\boldsymbol{R_i}} \big) + \sum_i^{N_e} \big(-\frac{\hbar^2}{2m_i} \nabla^2_{\boldsymbol{r_i}} \big) + \sum_{i,j} \big(-\frac{1}{4\pi\epsilon_0} \frac{e^2 Z_i}{|\boldsymbol{R}_i - \boldsymbol{r}_j|} \big) + \sum_{i \neq j} \big(-\frac{1}{8\pi\epsilon_0} \frac{e^2}{|\boldsymbol{r}_i - \boldsymbol{r}_j|} \big) + \sum_{i \neq j} \big(-\frac{1}{8\pi\epsilon_0} \frac{e^2 Z_i Z_j}{|\boldsymbol{R}_i - \boldsymbol{R}_j|} \big). \quad (2.12)$$

It is impossible to solve this problem exactly. Let us take the Born-Oppenheimer approximation, which states that the nuclei are much heavier and slower than the electrons and thus they stay at fixed positions. Then, the first term of (2.12) vanishes and the last term shifts the solution by a constant value. As a result we obtain:

$$\hat{H} = \hat{T} + \hat{V} + \hat{U}, \quad (2.13)$$

where $\hat{V}$ is system-specific and describves the crystal potential and $\hat{U}$ is an electron-electron interaction term.

As this does not make the problem exactly solvable, it may be treated further on the basis of the *Hohenberg-Kohn theorems*. The first Hohenberg-Kohn theorem states that the external potential $V(\boldsymbol{r})$, and hence the total energy of the system, is a unique functional of the electron density $n(\boldsymbol{r})$. Therefore, the energy functional $E[n(\boldsymbol{r})]$ may be expressed as:

$$E[n(\boldsymbol{r})] = \langle \Psi | \, \hat{H} \, | \Psi \rangle = \int n(\boldsymbol{r}) V(\boldsymbol{r}) d\boldsymbol{r} + F[n(\boldsymbol{r})], \quad (2.14)$$

where the universal functional $F[n(\boldsymbol{r})]$ is given by

$$\hat{F} = \hat{T} + \hat{U}. \quad (2.15)$$

The second Hohenberg-Kohn theorem states that the electronic density minimising the total energy is the groundstate density and therefore, the groundstate energy can be obtained variationally. This means that, if only the functional $F[n(\boldsymbol{r})]$ is known, by minimising the total energy we may obtain the groundstate density $n(\boldsymbol{r})$ corresponding to the external potential $V(\boldsymbol{r})$.

Since the exact expression for $F[n(\boldsymbol{r})]$ is not known, the real calculations are determined by the *Kohn-Sham equations*. In the Kohn-Sham approach we imagine a system of non-interacting electrons yielding the same density as the studied physical system. The groundstate functional $F[n(\boldsymbol{r})]$ can be then expressed as

$$F[n] = T_s[n] + U_H[n] + E_{XC}[n], \quad (2.16)$$

where the functional $T_s[n]$ is the kinetic energy of the non-interacting system and the second part of the expression is the *Hartree energy* - a classical interacting term, corresponding to the wavefunction constructed as a product of single-particle states. The last term of the expression given by (2.16) is the exchange-correlation energy, which takes into account the quantum electron-electron repulsion due to Pauli's exclusion principle (exchange energy) and the correlation energy being the remaining unkown part of the functional $F[n]$:

$$E_c = F[n] - T_s[n] - U_H[n] - E_X. \quad (2.17)$$

Finding a reliable approximation of the exchange-correlation functional is the goal of the practical density functional theory methods.

We now can solve the problem of non-interacting particles in some potential $v_s(\mathbf{r})$ described by the Kohn-Sham (K-S) equation :

$$\left(-\frac{1}{2}\nabla^2 + v_s(\boldsymbol{r}) \right)\phi_i(\boldsymbol{r}) = \epsilon_i \phi_i(\boldsymbol{r}), \tag{2.18}$$

where

$$v_s(\boldsymbol{r}) = V(\boldsymbol{r}) + \int d^3r' \frac{n(\boldsymbol{r'})}{|\boldsymbol{r} - \boldsymbol{r'}|} + v_{XC}[n](\boldsymbol{r}) \tag{2.19}$$

and

$$U_H[n] = \int d^3r' \frac{n(\boldsymbol{r'})}{|\boldsymbol{r} - \boldsymbol{r'}|}. \tag{2.20}$$

It is important to note that the variational solving of the equation (2.18) requires a self-consistent procedure. It begins with the initial density guess for the non-interacting system, which determines the potential $v_s[n]$. Then, the K-S equation can be solved and the obtained density is compared with the last step. If no changes are detected in the following cycles, the density is taken to be the ground-state density, minimising the energy functional for the physical-system:

$$E[n] = \langle \Psi[n] | \, \hat{T} + \hat{V}_s \, | \Psi[n] \rangle \, . \tag{2.21}$$

There exist many approximations to the exchange-correlation functional. One of them is the local denisty approximation (LDA) which takes:

$$E_{XC}^{LDA} = \int d\boldsymbol{r} f(n(\boldsymbol{r})), \tag{2.22}$$

where $f(n)$ is some function of n. In this work the local spin density approximation (LSDA) is used, which is the spin-scaled generalisation of LDA and allows for spin-resolved calculations. Some other approximations include the generalised gradient approximation (GGA) expressing the E_{XC} as depending also on the gradients of the density n, altough it is not considered here.

2.2.2 Computational details.

The results of calculations of the electronic and magnetic properties of TMDCs nanostructures shown in section 3.2 are based on the first-principle plane-wave calculations obtained with the Abinit package.

An essesntial element in every DFT calculation is the usage of effective core potntials for atoms, called *pseudopotnetials*. In this work, Hartwigsen-Goedecker-Hutter (HGH) pseudopotentials [106] and projector augmented wave (PAW) potentials have been used [107]. The HGH pseudopotentials represent the norm-conserving class of pseudopotentials created in the context of the LDA approximation, while the PAWs are obtained with the Projector-Augmented Wave transformation and provide much gain in the efficiency of the calculations [107, 108].

A plane-wave basis set with the energy cutoff of 2200 eV is used with the norm-conserving pseudopotentials [109] and of 600 eV - with the PAWs [108]. This parameter determines the size of the basis set by inlcuding only the waves of the energy lower than the set energy cutoff. Detailed convergence studies of this parameter were performed prior to the calculations (example run shown in 18a). The exchange-correlation potential

is approximated in the LDA approximation both for spin-polarised and spin-unpolarised cases.

All structures are treated with the periodic boundary conditions with 10 Å of spacing between the planes in z and x direction to prevent their interaction. In the self-consistent total energy calculations BZ is sampled by 14 x 1 x 1 special k-points within the Monkhorst-Pack scheme [110], and number of these k-points was identified in the convergence studies (example run shown in 18b).

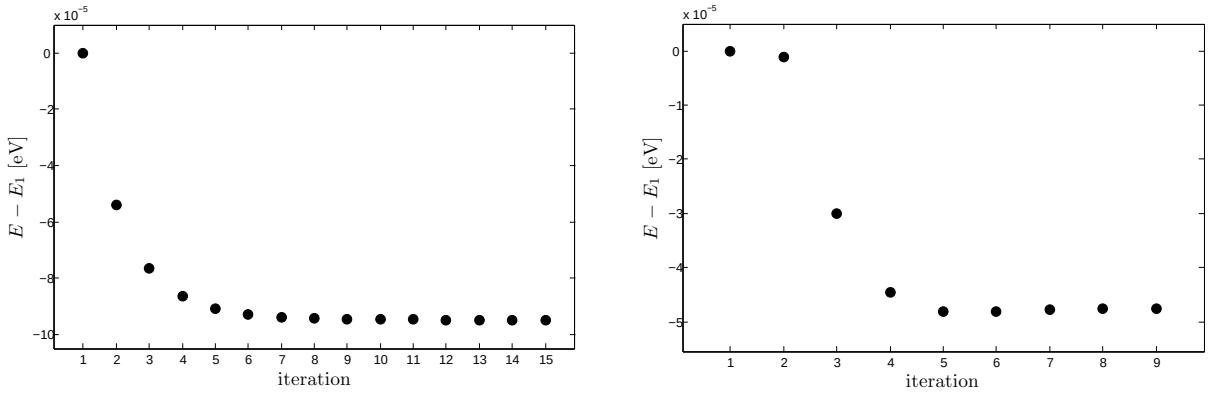

(a) **(b)**

Figure 18 – Convergence studies of MoS_2 monolayer in the Abinit package. (a) The convergence of the energy cutoff parameter. (b) The convergence of the number of k-point samples of the Brillouin zone. All energies are shown with respect to the first-iteration total energy.

3 Results.

In this chapter all the results obtained for nanostructures of TMDCs are presented. Section 3.1 includes the analysis of monolayers and nanoribbons of various TMDCs with the three-band tight-binding model, details for which are provided in the section 2.1.2. We consider also spin-orbit coupling (SOC) effects. Later, properties of MoSSe nanoribbons (NRs) are discussed and the results produced within density functional methods are given in the second section of this chapter. Details of these calculations are listed in the section 3.2.

3.1 Tight-binding model for TMDC nanostructures.

The calculations have been performed for various TMDC monolayers and for MoS2 nanoribbons in order to obtain their band structures and determine the validity of the model simplifications.

3.1.1 2D TMDC monolayers.

The studies of TMDC monolayers in three-band TB model include implementation of Hamiltonian derived for single-layer MX_2 crystal lattice and expressed in the three-band basis for only nearest-neighbours (NN) **d-d** hoppings. Initially we do not consiter SOC. For a infinite MoS_2 monolayer we obtain the following Hamiltonian

$$H^{NN}(k_x, k_y)_{2D} = \begin{pmatrix} h_0 & h_1 & h_2 \\ h_1^\dagger & h_{11} & h_{12} \\ h_2^\dagger & h_{12}^\dagger & h_{22} \end{pmatrix}, \tag{3.1}$$

where $h_{ij} = h_{ij}(k_x, k_y)$ are angle-dependent hopping integrals for orbitals i, j. The NN Hamiltonian has dimensions 3×3 as we take 3 orbitals from one metal atom in every unit cell into account (shown in Fig. 19).

Following G.B.Liu *et al.* [39], the expressions for matrix elements $h_{ij}(\alpha, \boldsymbol{k})$ have been derived:

$$h_0 = 2t_0(\cos 2\alpha + 2\cos\alpha\cos\beta) + \epsilon_1, \tag{3.2}$$

$$h_1 = -2\sqrt{3}t_2 \sin\alpha \sin\beta + 2it_1(\sin 2\alpha + \sin\alpha\cos\beta), \tag{3.3}$$

$$h_2 = 2t_2(\cos 2\alpha - \cos\alpha\cos\beta) + 2\sqrt{3}it_1\cos\alpha\sin\beta, \tag{3.4}$$

$$h_{11} = 2t_{11}\cos 2\alpha + (t_{11} + 3t_{22})\cos\alpha\cos\beta + \epsilon_2, \tag{3.5}$$

$$h_{22} = 2t_{22}\cos 2\alpha + (3t_{11} + t_{22})\cos\alpha\cos\beta + \epsilon_3, \tag{3.6}$$

$$h_{12} = \sqrt{3}(t_{22} - t_{11})\sin\alpha\sin\beta + 4it_{12}\sin\alpha(\cos\alpha - \cos\beta), \tag{3.7}$$

where

$$(\alpha, \beta) = \left(\frac{1}{2}k_x a, \frac{\sqrt{3}}{2}k_y a\right) \tag{3.8}$$

and ϵ_j is an on-site energy for an atomic orbital $|\phi_j\rangle$ (and $\epsilon_2 = \epsilon_3$) and the hopping integrals between the atomic orbitals are given by

$$t_0 = \langle\phi_0(\mathbf{0})|\,\hat{H}\,|\phi_0(\boldsymbol{R_1})\rangle\,, \tag{3.9}$$

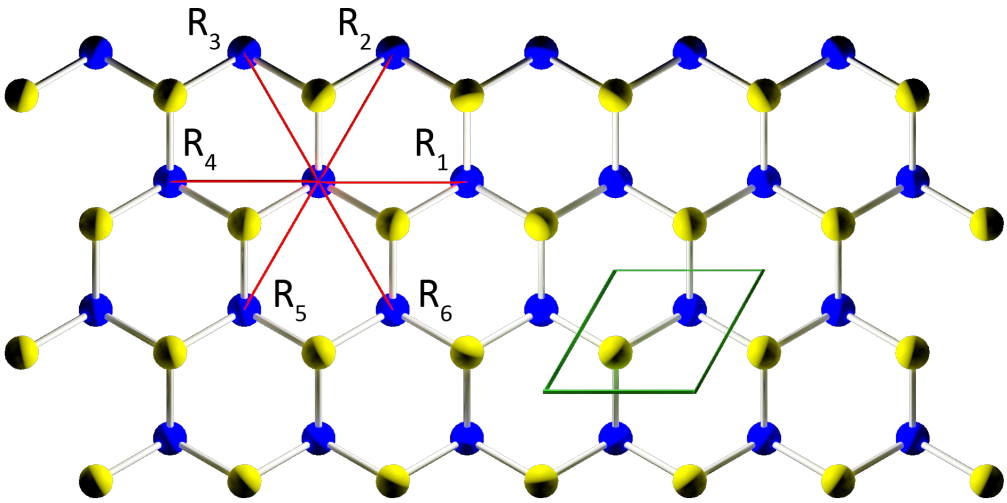

Figure 19 – Top view of a monolayer TMDC crystal's honeycomb lattice. Blue balls denote metal atoms and yellow balls - chalcogen atoms. The unit cell consisting of three atoms (one metal atom and three chalcogen atoms) is shown in green. In fact, only metal atom contribution is taken into account in the three-band model from every unit cell, while chalcogen atoms contribution is neglected. Relative positions of nearest-neighbouring metal atoms are shown in red and denoted R_i.

$$t_1 = \langle \phi_0(\mathbf{0}) | \hat{H} | \phi_1(\boldsymbol{R_1}) \rangle , \tag{3.10}$$

$$t_2 = \langle \phi_1(\mathbf{0}) | \hat{H} | \phi_1(\boldsymbol{R_1}) \rangle , \tag{3.11}$$

$$t_{11} = \langle \phi_0(\mathbf{0}) | \hat{H} | \phi_2(\boldsymbol{R_1}) \rangle , \tag{3.12}$$

$$t_{12} = \langle \phi_1(\mathbf{0}) | \hat{H} | \phi_2(\boldsymbol{R_1}) \rangle , \tag{3.13}$$

$$t_{22} = \langle \phi_2(\mathbf{0}) | \hat{H} | \phi_2(\boldsymbol{R_1}) \rangle , \tag{3.14}$$

atomic site $\boldsymbol{R_1}$ is shown in Fig. 19 and the values of t are given in Tab. 1:

	ϵ_1	ϵ_2	t_0	t_1	t_2	t_{11}	t_{12}	t_{22}
MoS_2	1.046	2.104	−0.184	0.401	0.507	0.218	0.338	0.057
WS_2	1.130	2.275	−0.206	0.567	0.536	0.286	0.384	−0.061
$MoSe_2$	0.919	2.065	−0.188	0.317	0.456	0.211	0.290	0.130
WSe_2	0.943	2.179	−0.207	0.457	0.486	0.263	0.329	0.034
$MoTe_2$	0.605	1.972	−0.169	0.228	0.390	0.207	0.239	0.252
WTe_2	0.606	2.102	−0.175	0.342	0.410	0.233	0.270	0.190

Table 1 – Values of the parameters used in the NN TB model [39].

Hopping integrals to other neighbouring sites can be generated on the basis on the crystal symmetry resulting in the Hamiltonian form given by (3.1). The hopping integrals t are parameters of this model and their values from ref. [39] are taken in the calculations.

By diagonalisation of the Hamiltonian (3.1) in the three-band basis given by (2.9) for varying $\boldsymbol{k}$ we obtain the band structures for MX_2 (M=Mo,W; X=S,Se,Te) shown in Fig. 20, with the band gaps equal to: 1.656 eV, 1.806 eV, 1.436 eV, 1.540 eV, 1.070 eV, 1.067 eV for MoS_2, WS_2, $MoSe_2$, WSe_2, $MoTe_2$ and WTe_2 respectively.

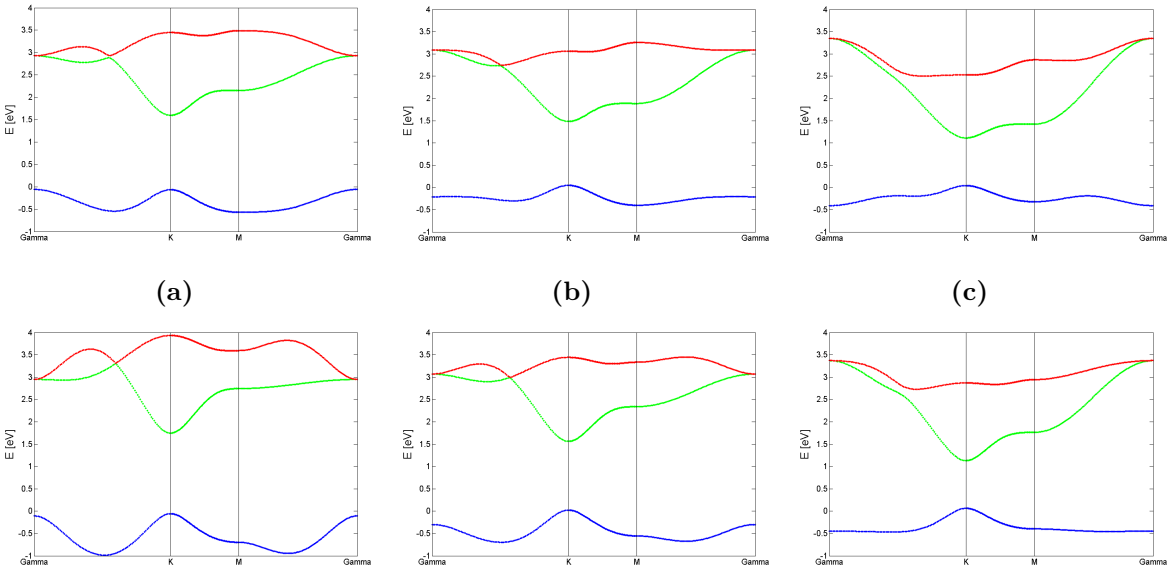

Figure 20 – Band structures obtained for monolayer TMDC crystals: MoS_2, $MoSe_2$, $MoTe_2$, WS_2, WSe_2 and WTe_2 in (a-f) respectively. Colors denote the three bands obtained within the model.

In order to obtain more accurate model for calculating the band structure we include the third-nearest-neighbour (TNN) hoppings. The resulting Hamiltonian reads:

$$H^{TNN}(k_x, k_y)_{2D} = \begin{pmatrix} v_0 & v_1 & v_2 \\ v_1^\dagger & v_{11} & v_{12} \\ v_2^\dagger & v_{12}^\dagger & v_{22} \end{pmatrix}, \tag{3.15}$$

where $v_{ij} = v_{ij}(k_x, k_y)$ are angle-dependent hopping integral matrices for orbitals i, j. Following G.B.Liu *et al.* [39], the expressions for matrix elements $v_{ij}(\alpha, \boldsymbol{k})$ have been derived:

$$v_0 = \epsilon_1 + 2t_0(\cos 2\alpha + 2\cos\alpha\cos\beta) + 2r_0(2\cos 3\alpha\cos\beta + \cos 2\beta) + 2u_0(2\cos 2\alpha\cos 2\beta + \cos 3\alpha), \tag{3.16}$$

$$Re(v_1) = -2\sqrt{3}t_2\sin\alpha\sin\beta + 2(r_1 + r_2)\sin 3\alpha\sin\beta - 2\sqrt{3}u_2\sin 2\alpha\sin 2\beta, \tag{3.17}$$

$$Im(v_1) = 2t_1\sin\alpha(2\cos\alpha + \cos\beta) + 2(r_1 - r_2)\sin 3\alpha\cos\beta + 2u_1\sin 2\alpha(2\cos 2\alpha + \cos 2\beta) \tag{3.18}$$

$$Re(v_2) = 2t_2(\cos 2\alpha - \cos\alpha\cos\beta) - \frac{2}{\sqrt{3}}(r_1 + r_2)\cos 3\alpha\cos\beta - \cos 2\alpha) + 2u_2(\cos 4\alpha - \cos 2\alpha\cos 2\beta), \tag{3.19}$$

$$Im(v_2) \quad = \quad 2\sqrt{3}t_1 \cos\alpha \sin\beta \; + \; \frac{2}{\sqrt{3}} \sin\beta(r_1 \; - \; r_2)(\cos 2\alpha \; + \; 2\cos\beta), \quad (3.20)$$

$$v_{11} = \epsilon_2 + 2t_{11}\cos 2\alpha + (t_{11} + 3t_{22})\cos\alpha\cos\beta + 2t_{11}\cos 2\alpha + 4r_{11}\cos 3\alpha\cos\beta + 2(r_{11} + \sqrt{3}r_{12})\cos 2\beta + (u_{11} + 3u_{22}\cos 2\alpha\cos 2\beta + 2u_{11}\cos 4\alpha), \quad (3.21)$$

$$v_{22} = \epsilon_3 + 2t_{22}\cos 2\alpha + (3t_{11} + t_{22})\cos\alpha\cos\beta + 2t_{22}\cos 2\alpha + 2r_{11}(2\cos 3\alpha\cos\beta + \cos 2\beta) + \frac{2}{\sqrt{3}}r_{12}(4\cos 3\alpha\cos\beta - \cos 2\beta) + (3u_{11} + u_{22}\cos 2\alpha\cos 2\beta + 2u_{22}\cos 4\alpha), \quad (3.22)$$

$$Re(v_{12}) = \sqrt{3}(t_{22} - t11)\sin\alpha\sin\beta + 4r_{12}\sin 3\alpha\sin\beta + \sqrt{3}(u_{22} - u_{11}\sin 2\alpha\sin 2\beta), \quad (3.23)$$

$$Im(v_{12}) \quad = \quad 4t_{12}\sin\alpha(\cos\alpha \; - \; \cos\beta) \; + \; 4u_{12}\sin 2\alpha(\cos 2\alpha \; - \; \cos 2\beta), \quad (3.24)$$

where (α, β) and ϵ_j are defined by (3.8) and the hopping integrals between the atomic orbitals (for $\boldsymbol{R_1}$ and $\boldsymbol{R_2}$ shown in Fig. 19) are given by:

$$r_0 = \langle\phi_0(\mathbf{0})|\,\hat{H}\,|\phi_0(\boldsymbol{R_1} + \boldsymbol{R_2})\rangle\,, \quad (3.25)$$
$$r_1 = \langle\phi_0(\mathbf{0})|\,\hat{H}\,|\phi_1(\boldsymbol{R_1} + \boldsymbol{R_2})\rangle\,, \quad (3.26)$$
$$r_2 = \langle\phi_1(\mathbf{0})|\,\hat{H}\,|\phi_1(\boldsymbol{R_1} + \boldsymbol{R_2})\rangle\,, \quad (3.27)$$
$$r_{11} = \langle\phi_0(\mathbf{0})|\,\hat{H}\,|\phi_2(\boldsymbol{R_1} + \boldsymbol{R_2})\rangle\,, \quad (3.28)$$
$$r_{12} = \langle\phi_1(\mathbf{0})|\,\hat{H}\,|\phi_2(\boldsymbol{R_1} + \boldsymbol{R_2})\rangle\,, \quad (3.29)$$
$$r_{22} = \langle\phi_2(\mathbf{0})|\,\hat{H}\,|\phi_2(\boldsymbol{R_1} + \boldsymbol{R_2})\rangle\,, \quad (3.30)$$
$$u_0 = \langle\phi_0(\mathbf{0})|\,\hat{H}\,|\phi_0(2\boldsymbol{R_1})\rangle\,, \quad (3.31)$$
$$u_1 = \langle\phi_0(\mathbf{0})|\,\hat{H}\,|\phi_1(2\boldsymbol{R_1})\rangle\,, \quad (3.32)$$
$$u_2 = \langle\phi_1(\mathbf{0})|\,\hat{H}\,|\phi_1(2\boldsymbol{R_1})\rangle\,, \quad (3.33)$$
$$u_{11} = \langle\phi_0(\mathbf{0})|\,\hat{H}\,|\phi_2(2\boldsymbol{R_1})\rangle\,, \quad (3.34)$$
$$u_{12} = \langle\phi_1(\mathbf{0})|\,\hat{H}\,|\phi_2(2\boldsymbol{R_1})\rangle\,, \quad (3.35)$$
$$u_{22} = \langle\phi_2(\mathbf{0})|\,\hat{H}\,|\phi_2(2\boldsymbol{R_1})\rangle \quad (3.36)$$

and the expressions for t are given by 3.9-3.14 (with values of all parameters t, u, r listed in Tab. 2).

	ϵ_1	ϵ_2	t_0	t_1	t_2	t_{11}	t_{12}	t_{22}	r_0	
	r_2	r_{11}	r_{12}	u_0	u_1	u_2	u_{11}	u_{12}	u_{22}	r_1
					GGA					
MoS_2	0.683	1.707	−0.146	−0.114	0.506	0.085	0.162	0.073	0.060	−0.236
	0.067	0.016	0.087	−0.038	0.046	0.001	0.266	−0.176	−0.150	
WS_2	0.717	1.916	−0.152	−0.097	0.590	0.047	0.178	0.016	0.069	−0.261
	0.107	−0.003	0.109	−0.054	0.045	0.002	0.325	−0.206	−0.163	
$MoSe_2$	0.684	1.546	−0.146	−0.130	0.432	0.144	0.117	0.075	0.039	−0.209
	0.069	0.052	0.060	−0.042	0.036	0.008	0.272	−0.172	−0.150	
WSe_2	0.728	1.655	−0.146	−0.124	0.507	0.117	0.127	0.015	0.036	−0.234
	0.107	0.044	0.075	−0.061	0.032	0.007	0.329	−0.202	−0.164	
$MoTe_2$	0.588	1.303	−0.226	−0.234	0.036	0.400	0.098	0.017	0.003	−0.025
	−0.169	0.082	0.051	0.057	0.103	0.187	−0.045	−0.141	0.087	
WTe_2	0.697	1.380	−0.109	−0.164	0.368	0.204	0.093	0.038	−0.015	−0.209
	0.107	0.115	0.009	−0.066	0.011	−0.013	0.312	−0.177	−0.132	

Table 2 – Values of parameters used in the TNN TB model [39].

The TNN Hamiltonian is diagonalised for varying $\boldsymbol{k}$ in the three-band basis given again by (2.9) and the resulting band structure for MoS_2 is shown in Fig. 21a in comaprison to the NN band structure. They differ in most of the Brillouin zone (BZ) except for the $\boldsymbol{K}$ point where the bands reach their extrema. Band curvatures and band gaps there are very similar. The band gap obtained in this approximation for MoS_2 is 1.598 eV. The band structure and the band gap value compare well to the result given in literature [111, 112].

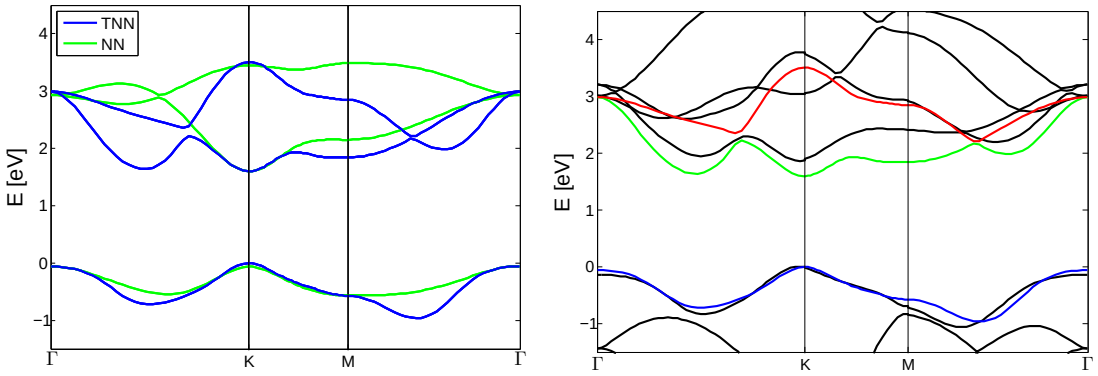

(a) **(b)**

Figure 21 – (a) A comparison of the NN (green) and TNN (blue) three-band TB model results of band structure of MoS_2 monolayer. (b) A comparison of the band structure of MoS_2 obtained in the TNN three-band TB model (color lines) and with DFT methods in Abinit package (black lines).

Additionally, in order to obtain detailed comparison of the results of the model discussed here, calculations with density functional theory (DFT) methods have been performed with the use of the Abinit package. A comparison of these results to the band structure obtained within the three-band model is shown in Fig. 21b. There is no perfect agreement between these results, although the model reproduces the valence band (especially in the $\boldsymbol{K}$ point) and captures reasonably well the curvatures of the other bands. The band gap mismatch may be originated both in the TB model faults and the inaccuracy of the LDA approximation to DFT methods. This proves that the model investigated here is fairly sufficient to capture the low-energy properties of TMDC monolayers, if only the third-nearest-neighbour contributions are taken into account.

3.1.2 Effect of spin-orbit coupling.

While investigating a TB model for TMDC nanostructures it is important to consider the valley properties of these materials. Such a model should take into account the spin splitting of the bands that is reversed in the two inequvalent valleys of BZ. This is especially vital due to the large SOC observed in TMDCs. In order to study this effect we incorporate the SOC term in our effective Hamiltonian, considering only the on-site contributions, namely including only terms originated at Mo atoms. We express the Hamiltonian in the basis

$$\{|d_{z^2},\uparrow\rangle, |d_{xy},\uparrow\rangle, |d_{x^2-y^2},\uparrow\rangle, |d_{z^2},\downarrow\rangle, |d_{xy},\downarrow\rangle, |d_{x^2-y^2},\downarrow\rangle\} \tag{3.37}$$

and the SOC term in the Hamiltonian has the form [39]:

$$\hat{H}' = \lambda \boldsymbol{L}\cdot\boldsymbol{S} = \frac{\lambda}{2}\begin{pmatrix} L_z & 0 \\ 0 & L_z \end{pmatrix}, \qquad \text{where} \quad L_z = \begin{pmatrix} 0 & 0 & 0 \\ 0 & 0 & 2i \\ 0 & -2i & 0 \end{pmatrix} \tag{3.38}$$

and L_z is the matrix of z component of the orbital angular momentum and λ characterises the strength of the SOC. Therefore, the full Hamiltonian has the form:

$$H^{\hat{SOC}} = I \otimes \hat{H}(\boldsymbol{k}) + \hat{H}' = \begin{pmatrix} \hat{H}(\boldsymbol{k}+\frac{\lambda}{2}L_z) & 0 \\ 0 & \hat{H}(\boldsymbol{k}-\frac{\lambda}{2}L_z) \end{pmatrix}, \tag{3.39}$$

where I is identity matrix and $\hat{H}(\boldsymbol{k})$ is a NN or TNN Hamiltonian. The Hamiltonian given by 3.39 is block-diagonal, therefore the z components of spin s_z are not mixed and hence this a good quantum number. From the SOC Hamiltonian we can predict the spin-splitting of the bands. Because the SOC Hamiltonian affects only bands formed of $|\phi_2\rangle$ and $|\phi_3\rangle$, that is of $|d_{xy}\rangle$ and $|d_{x^2-y^2}\rangle$ orbitals - we might expect a large splitting of the valence band (VB) in **K** point (equal to 2λ [19, 39]) but since the conduction band (CB) is formed of the $|d_{z^2}\rangle$ orbitals - there will be no splitting in its minimum in **K** point. There is no spin splitting in the Γ or M points for any band. This is comparable to the spin-splitting studies given in literature [19].

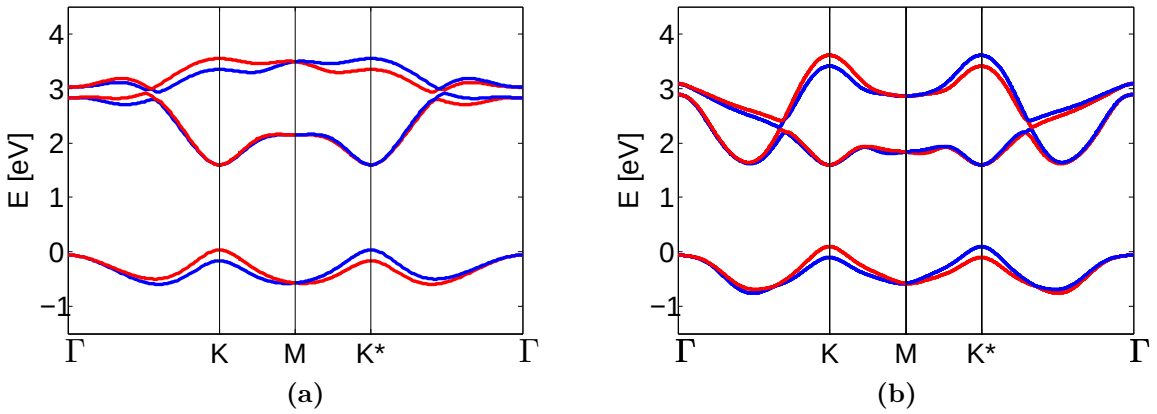

Figure 22 – Band structure of MoS_2 monolayer with spin-orbit coupling implemented in the (a) NN and (b) TNN TB model. Spin splitting of the bands exists only in the $\boldsymbol{K}$ and $\boldsymbol{K'}$ points, where the spin valence bands are flipped for the opposite valleys.

The band structure obtained with the SOC Hamiltonian given by (3.39) is shown in Fig. 22 and the splitting in the two **K** and **K'** points is shown as well. We can observe the SOC splitting of the VB and the flip of the spin bands is apparent for the **K'** valley with respect to **K** point.

3.1.3 TMDC nanoribbons.

Since the three-band model has proven to give reasonable results for TMDC monolayers, it is important to study its ability to describe the properties of TMDC NRs. Therefore, Hamiltonians for zigzag- and armchair-edged NRs have been derived and expressed in the three-band basis given by (2.9). Only nearest-neighbour hopping terms between metal atoms were included as shown in Fig. 23.

We analyse zigzag-edged and armchair-edged NRs (shown in Fig. 19 and 23). In fact, since we consider only contribution from metal atoms, any effects associated with edge passivation will not be fully described. It is so as in such analysis we would have to include the orbitals of an atom that would passivate the Mo-edge, like sulphur or hydrogen. The S-edge on the other hand needs no passivation but its contribution is also neglected.

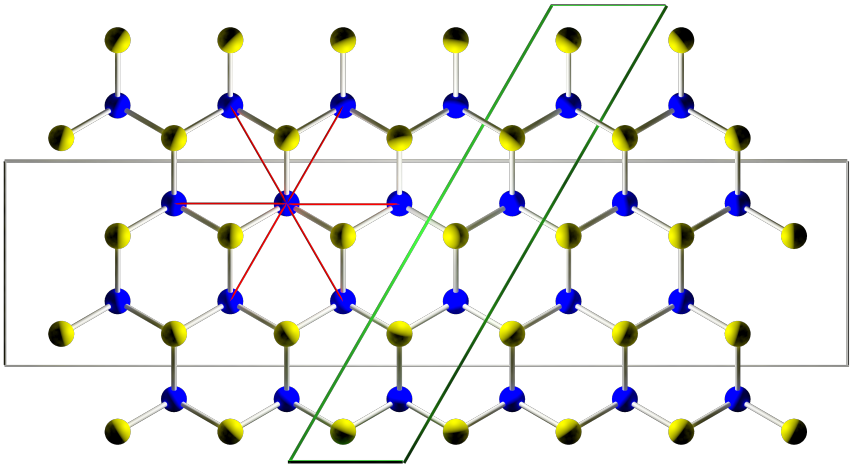

Figure 23 – Top view of the crystal structure of a MoS_2 nanoribbon. At the top of the picture the zigzag Mo-edge passivated with S atoms is shown. At the bottom of the picutre the zigzag S-edge is illustrated. Zigzag-edged (armchair-edged) NR extends infinitely to left and right (up and down) - the horizontal (vertical) edges are its zigzag (armchair) edges. The unit cells of a zigzag-edged (armchair-edged) NR is shown in green (grey). Distances to nearest neighbour metal atoms are shown in red.

For zigzag-edged nanoribbon (ZNR) we obtain:

$$H^{NN}_{1D,zigzag}(k_x) = \begin{pmatrix} h'_1 & h'^{\dagger}_2 & & & \\ h'_2 & h'_1 & h'^{\dagger}_2 & & \\ & h'_2 & h'_1 & \ddots & \\ & & \ddots & \ddots & h'^{\dagger}_2 \\ & & & h'_2 & h'_1 \end{pmatrix} \tag{3.40}$$

and the hopping matrices h_1 and h_2 have been derived, following G.B.Liu *et al.* [39]:

$$h_1' = \epsilon_i + e^{i\boldsymbol{kR_1}} \langle \phi_i(\mathbf{0})| \hat{H} |\phi_j(\boldsymbol{R_1})\rangle + e^{i\boldsymbol{kR_4}} \langle \phi_i(\mathbf{0})| \hat{H} |\phi_j(\boldsymbol{R_4})\rangle$$
$$= \begin{pmatrix} \epsilon_1 + 2\cos(k_x a)t_0 & 2i\sin(k_x a)t_1 & 2\cos(k_x a)t_2 \\ -2i\sin(k_x a)t_1 & \epsilon_2 + 2\cos(k_x a)t_{11} & 2i\sin(k_x a)t_1 2 \\ 2\cos(k_x a)t_2 & -2i\sin(k_x a)t_{12} & \epsilon_3 + 2\cos(k_x a)t_{22} \end{pmatrix}, \tag{3.41}$$

$$h_2' = e^{i\boldsymbol{kR_2}} \langle \phi_i(\mathbf{0})| \hat{H} |\phi_j(\boldsymbol{R_2})\rangle + e^{i\boldsymbol{kR_3}} \langle \phi_i(\mathbf{0})| \hat{H} |\phi_j(\boldsymbol{R_3})\rangle$$
$$= \begin{pmatrix} s_0 & s_1^+ & s_2^- \\ s_1^- & s_{11} & s_{12}^+ \\ s_2^+ & s_{12}^- & s_{22} \end{pmatrix}, \tag{3.42}$$

where $\boldsymbol{R_i}$ have been marked in Fig. 23, $|\phi_i(\boldsymbol{r})\rangle$ are given by (2.9) and

$$s_0 = 2\cos(\frac{1}{2}k_x a)t_0, \tag{3.43}$$

$$s_1^{\pm} = \pm i\sin(\frac{1}{2}k_x a)(t_1 \mp \sqrt{3}t_2), \tag{3.44}$$

$$s_2^{\pm} = \pm\frac{1}{2}\cos(\frac{1}{2}k_x a)(\sqrt{3}t_1 \mp t_2) \tag{3.45}$$

$$s_{11} = \frac{1}{2}\cos(\frac{1}{2}k_x a)(t_{11} + 3t_{22}), \tag{3.46}$$

$$s_{12}^{\pm} = -i\sin(\frac{1}{2}k_x a)(\frac{\sqrt{3}}{2}t_{11} \pm 2t_{12} - \frac{\sqrt{3}}{2}t_{22}), \tag{3.47}$$

$$s_{22} = \frac{1}{2}\cos(\frac{1}{2}k_x a)(3t_{11} + t_{22}) \tag{3.48}$$

and t, ϵ_j are given by 3.9-3.14 and listed in Tab. 1.

The Hamiltonian matrix for zigzag-edged NR has dimensions $3n \times 3n$ where n is the number of metal atoms in the lattice cell of a ZNR and 3 stands for the three-band basis. The elementary cell for a ZNR has been marked with green colour in Fig. 23. It is convenient to refer to NRs of different width using this number n: n-ZNR will be a zigzag-edged nanoribbon with n atoms in the elementary cell.

We obtain the band structure of ZNRs by diagonalising the Hamiltonian matrix in the three-band basis. Results for 15-ZNR are shown in Fig. 24 in comparison with the results from ref. [39]. It is apparent that the band gap in Γ or in the X point are not comparable. We also may conclude that some of the edge states appearing in the energy gap are reasonably well reproduced, whereas some other - are missing from the picture entirely. This is due to the fact that these states are formed of different orbitals, not taken into account in the three-band model [39].

For armchair nanoribbons (ANR) the Hamiltonian reads:

$$H^{NN}_{1D,armchair}(k_y) = \begin{pmatrix} E & y_1 & T^\dagger & & & & \\ y_1^\dagger & E & y_2^\dagger & T^\dagger & & & \\ T & y_2 & E & y_1 & T^\dagger & & \\ & T & y_1^\dagger & E & \ddots & \ddots & \\ & & T & \ddots & \ddots & \ddots & T^\dagger \\ & & & \ddots & \ddots & E & y_2^\dagger \\ & & & & T & y_2 & E \end{pmatrix}, \tag{3.49}$$

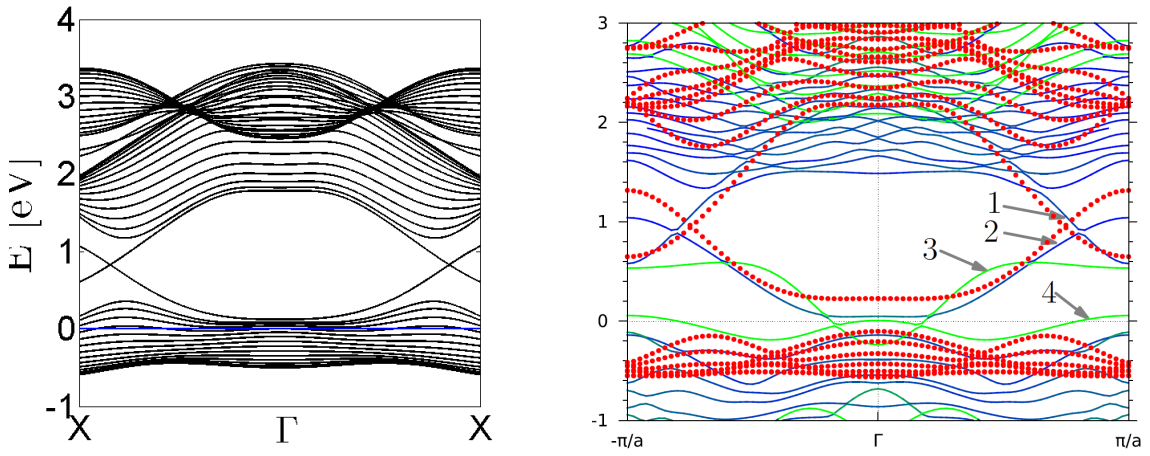

(a) **(b)**

Figure 24 – Band structure of a zigzag-edged MoS_2 nanoribbon of 15 metal atoms in the unit cell. (a) Results of NN three-band TB calculation and (b) comparison of the TB model results (dotted red lines) to bands obtained from DFT methods (solid lines) [39]. Blue colour denotes the bands formed of the orbitals taken in to account in the three-band TB model, while green denotes neglected orbitals. States in the gap numbered by 1-2 are reasonably well reproduced but states denoted by 3-4 are absent. This because they are formed of the orbitals other than ones considered in the threeband approximation.

where y_1, y_2 and T are hopping matrices and E is matrix of onsite energies of the form:

$$y_1 = e^{i\boldsymbol{kR_3}} \langle \phi_i(\mathbf{0})| \hat{H} |\phi_j(\boldsymbol{R_3})\rangle + e^{i\boldsymbol{kR_5}} \langle \phi_i(\mathbf{0})| \hat{H} |\phi_j(\boldsymbol{R_5})\rangle = \begin{pmatrix} f_0 & f_1^- & f_2^+ \\ f_1^+ & f_{11} & f_{12}^+ \\ f_2^- & f_{12}^- & f_{22} \end{pmatrix} \tag{3.50}$$

and

$$f_0 = 2t_0 \cos(k_y a), \tag{3.51}$$

$$f_1^{\pm} = \pm t_1 \cos(k_y a) - i t_2 \sqrt{3} \sin(k_y a), \tag{3.52}$$

$$f_2^{\pm} = \pm i \sin(k_y a)(\sqrt{3} t_1 - t_2), \tag{3.53}$$

$$f_{11} = \frac{1}{2}(t_{11} + 3t_{22}) \cos(k_y a), \tag{3.54}$$

$$f_{12}^{\pm} = \pm 2t_{12} \cos(k_y a) + i \frac{\sqrt{3}}{2}(t_{22} - t_{11}) \sin(k_y a), \tag{3.55}$$

$$f_{22} = 2(3t_{11} + t_{22}) \cos(k_y a) \tag{3.56}$$

and

$$y_2 = e^{i\boldsymbol{kR_2}} \langle \phi_i(\mathbf{0})| \hat{H} |\phi_j(\boldsymbol{R_2})\rangle + e^{i\boldsymbol{kR_6}} \langle \phi_i(\mathbf{0})| \hat{H} |\phi_j(\boldsymbol{R_6})\rangle = \begin{pmatrix} g_0 & g_1^+ g_2^+ & \\ g_1^- & g_{11} & g_{12}^- \\ g_2^- & g_{12}^+ & g_{22} \end{pmatrix}, \tag{3.57}$$

where $\boldsymbol{R_i}$ have been marked in 23 and

$$g_0 = f_0 = 2t_0 \cos(k_y a), \tag{3.58}$$

$$g_1^{\pm} = \pm t_1 \cos(k_y a) + i t_2 \sqrt{3} \sin(k_y a), \tag{3.59}$$

$$g_2^{\pm} = f_2^{\pm} = \pm i \sin(k_y a)(\sqrt{3} t_1 - t_2), \tag{3.60}$$

$$g_{11} = f_{11} = \frac{1}{2}(t_{11} + 3t_{22}) \cos(k_y a), \tag{3.61}$$

$$g_{12}^{\pm} = \pm 2t_{12} \cos(k_y a) - i \frac{\sqrt{3}}{2}(t_{22} - t_{11}) \sin(k_y a), \tag{3.62}$$

$$g_{22} = f_{22} = 2(3t_{11} + t_{22}) \cos(k_y a) \tag{3.63}$$

and

$$\begin{aligned} T = e^{i\boldsymbol{k}\boldsymbol{R_1}} \langle \phi_i(\boldsymbol{0}) | \hat{H} | \phi_j(\boldsymbol{R_1}) \rangle + e^{i\boldsymbol{k}\boldsymbol{R_4}} \langle \phi_i(\boldsymbol{0}) | \hat{H} | \phi_j(\boldsymbol{R_4}) \rangle \\ = \begin{pmatrix} t_0 & -t_1 & t_2 \\ t_1 & t_{11} & -t_{12} \\ t_2 & t_{12} & t_{22} \end{pmatrix}, \end{aligned} \tag{3.64}$$

where the hopping integrals t are listed in Tab. 1 and

$$E = \begin{pmatrix} \epsilon_1 & 0 & 0 \\ 0 & \epsilon_2 & 0 \\ 0 & 0 & \epsilon_3 \end{pmatrix}, \tag{3.65}$$

where $\epsilon_2 = \epsilon_3$ and their values are given in Tab. 1 as well.

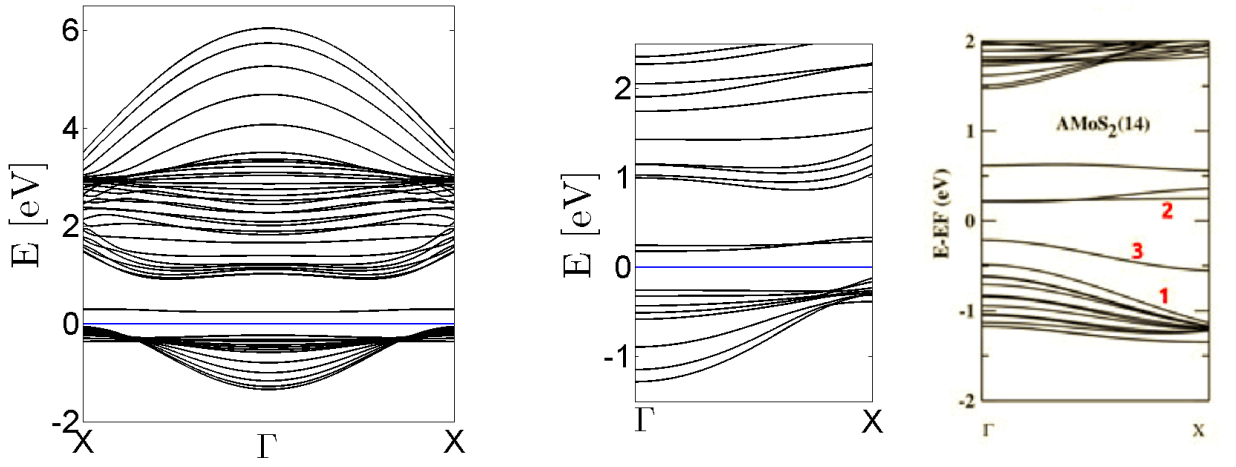

(a) **(b)** **(c)**

Figure 25 – Band structure of an armchair-edged MoS_2 nanoribbon of 15 metal atoms in the unit cell. (a) Results obtained in the three-band approximation to NN TB model. (b) a detailed fragment of (a) suited to comparison with (c). (c) Band structure obtained within DFT methods from ref. [93]. The state denoted by 2 is well reproduced by the TB calculations, but other states in the band gap are absent from the picture and the valence and conduction bands were not correctly reproduced in TB results either.

The Hamiltonian matrix for armchair-edged NR has dimensions $3m \times 3m$ where m is the number of metal atoms in the lattice cell of an ANR and 3 stands for the three-band basis. The elementary cell for an ANR has been marked with grey colour in Fig. 23. It is convenient to refer to NRs of different width using this number m: m-ANR will be a armchair-edged nanoribbon with m atoms in the elementary cell. We obtain the band structure of ANRs by diagonalising the Hamiltonian matrix in the three-band basis. Results for 15-ANR are shown in Fig. 25.

The results for three-band TB calculations for ANRs are shown in Fig. 24. The band structure for a 15-ANR has been shown in detail in order to compare to the results obtained in [93]. It is clearly visible that while some edge states apparent in the band gap are well reproduced (states marked with number 2 in Fig. 25), others - are absent from the figure. It is probably because of different orbitals forming the bands than the ones we have taken in the three-band model, as it was in case of ZNR. With this model the proper band curvatures or band gaps cannot be produced either.

3.1.4 Discussion.

The three-band TB model has been used in order to investigate the electronic properties of nanostructured TMDCs. It has been shown in section 3.1.1 that the model is sufficient to describe many important features of band structure of TMDC monolayers. In addition to similar band curvatures and existance of minima in $\boldsymbol{K}$ and $\boldsymbol{K'}$ points, it was possible to obtain the reverse-spin-split behaviour of the bands in the valleys with SOC taken into account in this model. In case of any low-energy calculations for TMDC monolayers the model is therefore adequate.

As for studies of TMDC NRs, although several edge states have been well reproduced, the model has proven to lack important contributions from other, non-metal and metallic (s, p) orbitals. This is concluded based on the absence of some edge states in the band gap that are crucial for understanding the properties of the NRs. Additionally, calculations performed within the model have not produced the correct band gaps or band curvatures. This is true for both ANRs and ZNRs. This suggests the necessity to include contributions from more orbitals in an extended model, which were neglected in this case. This way it might be possible to capture the differences between NRs with variable edge passivation, which is predicted to affects their studied properties considerably.

Also, since the three-band tight-binding model takes only three orbitals of metal atom into account and this has proven insufficient for the studies of NRs, it is predicted to fail to produce correct results for any 0-dimensional structures, such as quantum dots. This is due to immense importance of all-atom contribution in in the edge states, which very much determine their low energy properties. Therefore any calculations of such objects are not included in this work.

3.2 Density functional theory calculations of MoSSe nanoribbons.

This section provides the results of density functional theory calculations in Abinit package for various MoSSe nanoribbons. Detailed description of the NRs studied is given first and a geometry optimisation is presented in the following subsections. Later, the electronic and magnetic properties of chosen structures are discussed.

3.2.1 MoSSe nanoribbons under investigation.

The nanribbons studied include zigzag-edged narrow MoS_2, $MoSe_2$ and MoSSe nanoribbons of 2 and 4 metal atoms in the elementary cell (shown in Fig. 26). They will be refered to as 2-ZNR and 4-ZNR of the appropriate compounds. In calculations, the structures are defined with the elementary cell of 6 or 12 atoms, when chalcogen atoms need to be identified as well. Top and side views of the crytals analysed are shown in Fig. 26-27.

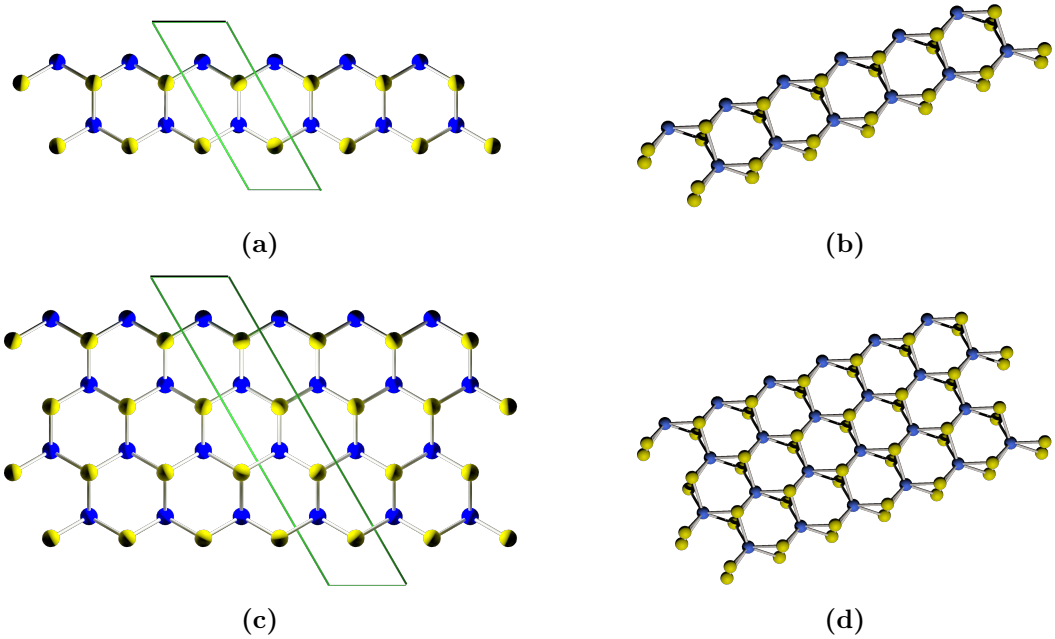

Figure 26 – Crystal structure of the zigzag-edged unpassivated MoS_2 nanoribbons under study. Top and 3D views include nanoribbons consisting of 2 (a-b) and 4 (c-d) Mo atoms in the unit cell. Unit cell is shown in green. Blue (yellow) balls represent Mo (S) atoms.

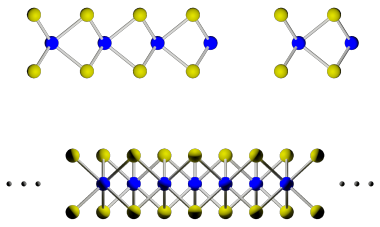

Figure 27 – Zigzag-edged unpassivated MoS_2 nanoribbons. Top left (right) picture represents a crosssection of a 4-Mo-atom wide (2-Mo-atom wide) NR. Bottom illustration shows a side view along the edge of a zigzag-edged NR. Blue (yellow) balls represent Mo (S) atoms.

Main factor of investigation has been the chalcogen coverage influence on the crystals' properties. 50% and 100% of S/Se coverage was considered, with different arrangement of atoms (shown in Fig. 29e). For distinction, in case of the two arrangements of chalcogens taken into consideration for 4-MoSSe-ZNRs we assign: 4a-MoSSe-ZNR for a structure shown in Fig. 28c with sulphur atoms near the edges and 4b-MoSSe-ZNR for a structure shown in Fig. 28d with selenium atoms near the edges.

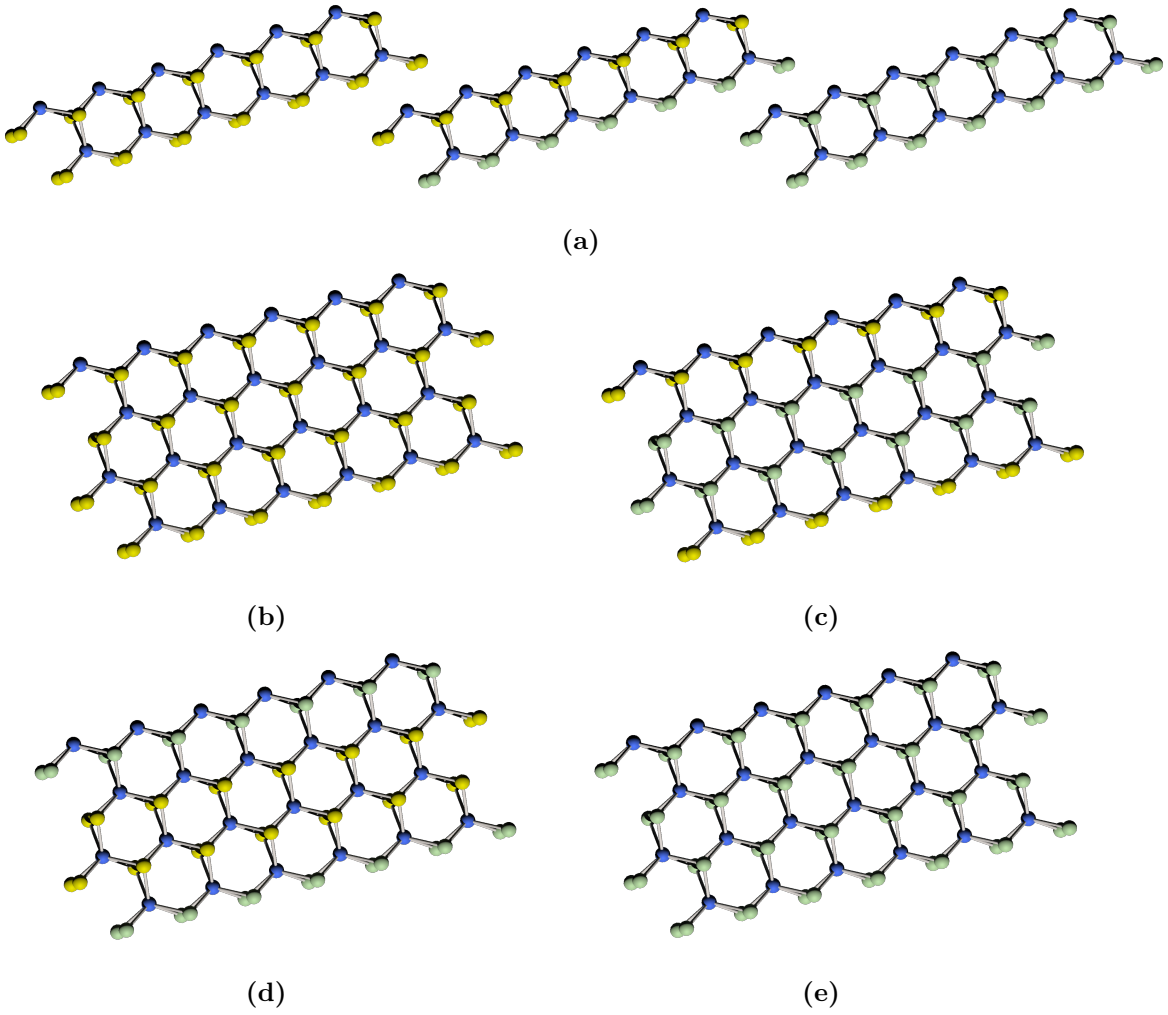

Figure 28 – Arrangement of S and Se atoms in the NRs under study. (a) From the left: $2-MoS_2$, $2-MoSSe$, $2-MoSe_2$ NR. (b-e) From (b) to (e): $4-MoS_2$, $4a-MoSSe$, $4b-MoSSe$, $4-MoSe_2$ NR. Blue balls represent Mo atoms and yellow (green) ones - S (Se) atoms.

3.2.2 Geometry optimisation.

In order to perform any calculations of the NRs properties it was needed to obtain their optimised geometry. The procedure was conducted with the minimisation of atomic forces with all the atoms allowed to move into more optimal positions. The latter condition proved necessary as such narrow NRs take forms much distorted with respect to ideal atom positions.

The obtained geometries are shown in cross-section images of electronic densities for all the studied structures in Fig. 29-30. Top and side views have been included to fully grasp

the changes in the crystal lattice. We may notice that MoS_2 NRs are the least distorted among NRs studied, which is true for any size. Furthermore, the Mo-edges differ more from the ideal shape than the S-edges, which occurs due to the lack of passivation. For most distorted crystals it is apparent that the Mo atoms close to the edges of NRs form a bond with each other.

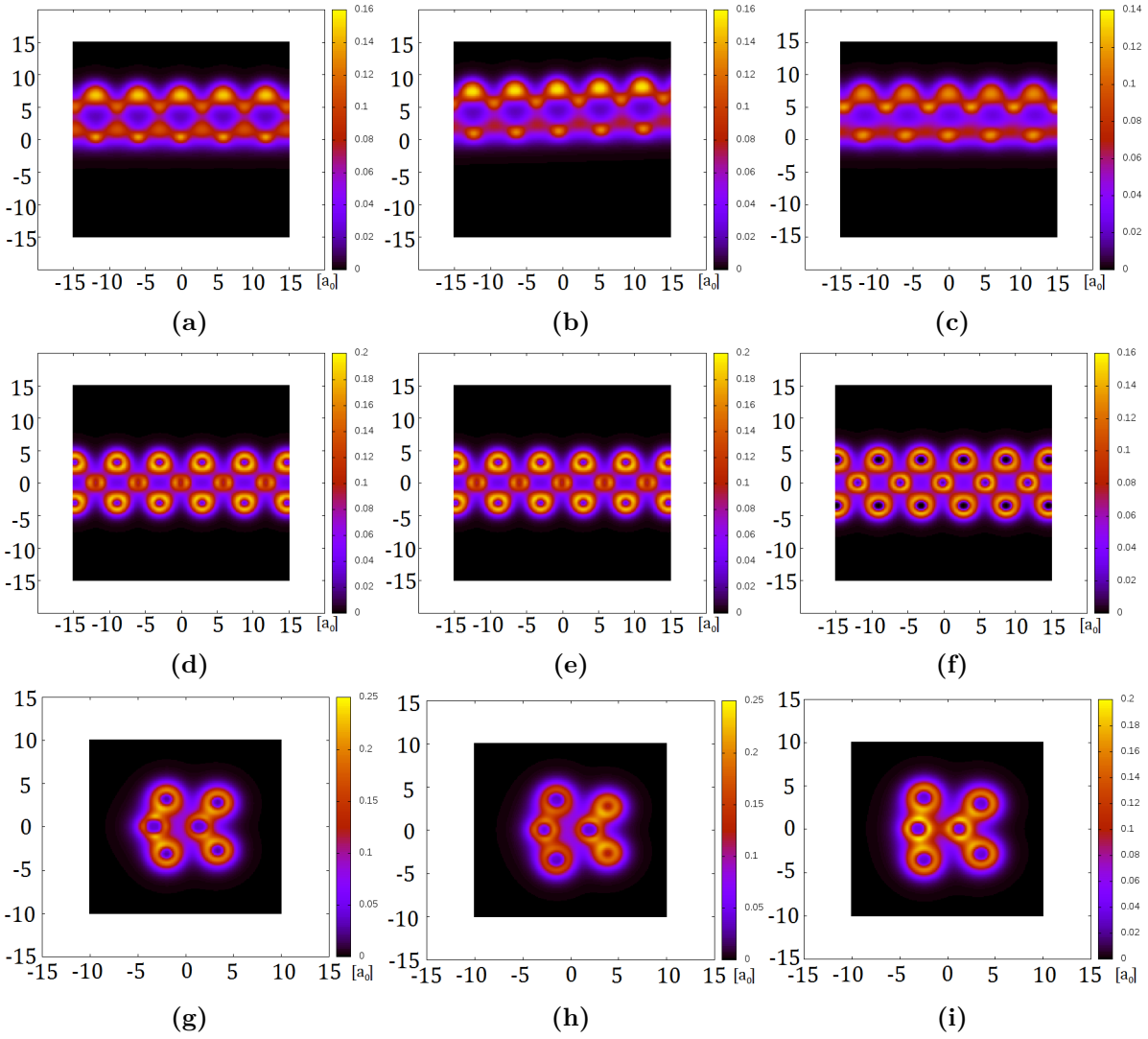

Figure 29 – Electronic densities of optimised 2-Mo-atom wide NRs. Columns show: from left: $2-MoS_2$, $2-MoSSe$, $2-MoSe_2$ NR. Rows show: from the top: top view, side view along the NR, crossection through a NR. MoS_2 NR shows the smallest distortion from the ideal lattice. The atoms on the Mo-edges of all NRs show strongest tendency to distort due to lack of passivation.

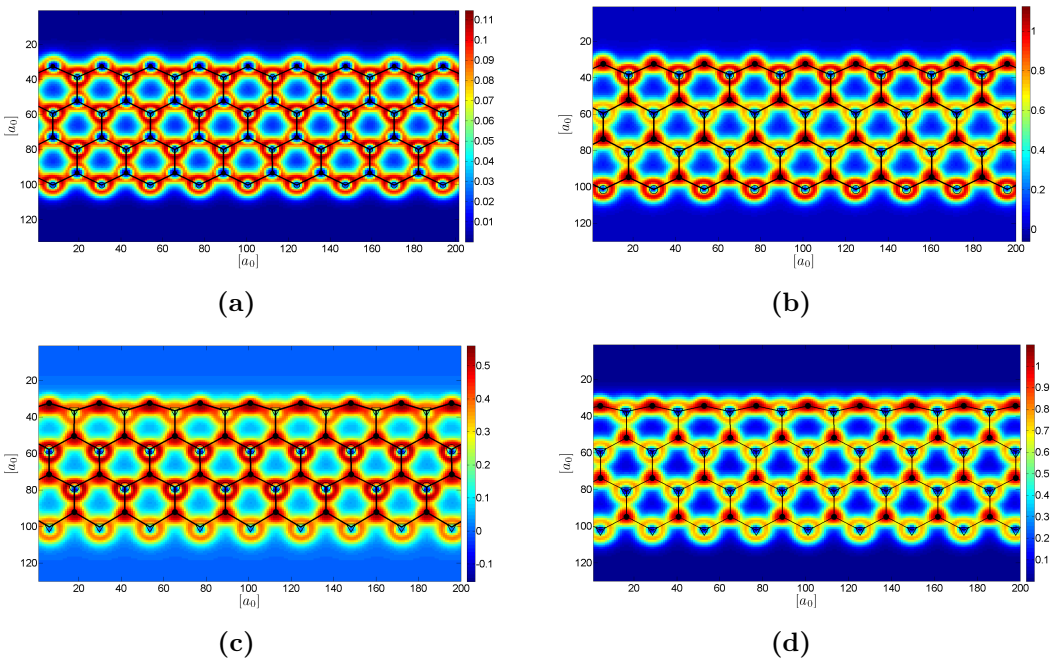

Figure 30 – Electronic densities of optimised 4-Mo-atom wide NRs: (a) $4 - MoS_2$, (b) $4a - MoSSe$, (c) $4b - MoSSe$, (d) $4 - MoSe_2$ NR. Optimised crystal lattice is shown for a clear picture. Full (empty) circles represent Mo (S) atoms and triangles stand for Se atoms.

Below the lattice constants for all the structures studied have been shown in Fig. 31. They vary significantly among NRs with different sulphur and selenium coverage. It is clear that for NRs of the same composition the lattice constant grows with size and the most extreme change occurs for MoSe2 NRs. At the same time, NRs of the mixed composition and different arrangements are characterised by similar lattice constants. For the constants obtained we may analyse the Mo-Mo distances, which vary between 3.041Å and 3.199Å, which is comparable to the results obtained in ref [77, 90]: $3.148 - 3.155$Å but for larger structures.

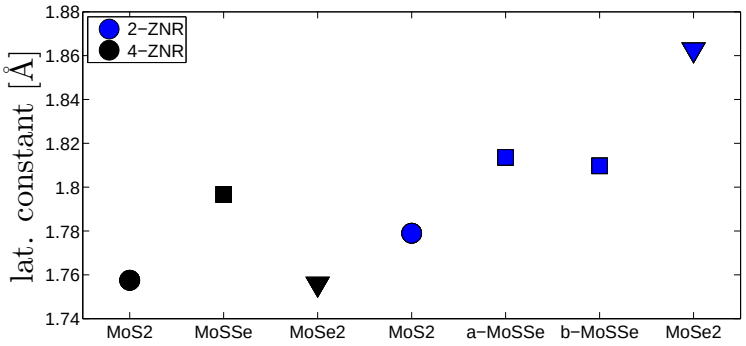

Figure 31 – Optimised lattice constants for the studied nanoribbons: black (blue) symbols denote 2-Mo-atom wide (4-Mo-atom wide) NRs. It can be seen that the MoS_2 NRs have smaller lattice constants and $MoSe_2$ - the largest. Lattice parameters grow with the NRs size, most rapidly - for $MoSe_2$ NRs. Regardless of the width of the NR, $MoSSe$ NRs do not differ significantly in terms of the lattice constants.

3.2.3 Electronic properties.

In order to investigate the electronic properties of the nanoribbons studied calculations of their band structure have been performed. The results are shown in Fig. 32. The band structures include a band gap of around 2.5 eV with edge states in the gap. The edge states cross each other in various points of BZ. We observe the semimetallic properties of the NR, as reported in literature [77, 90].

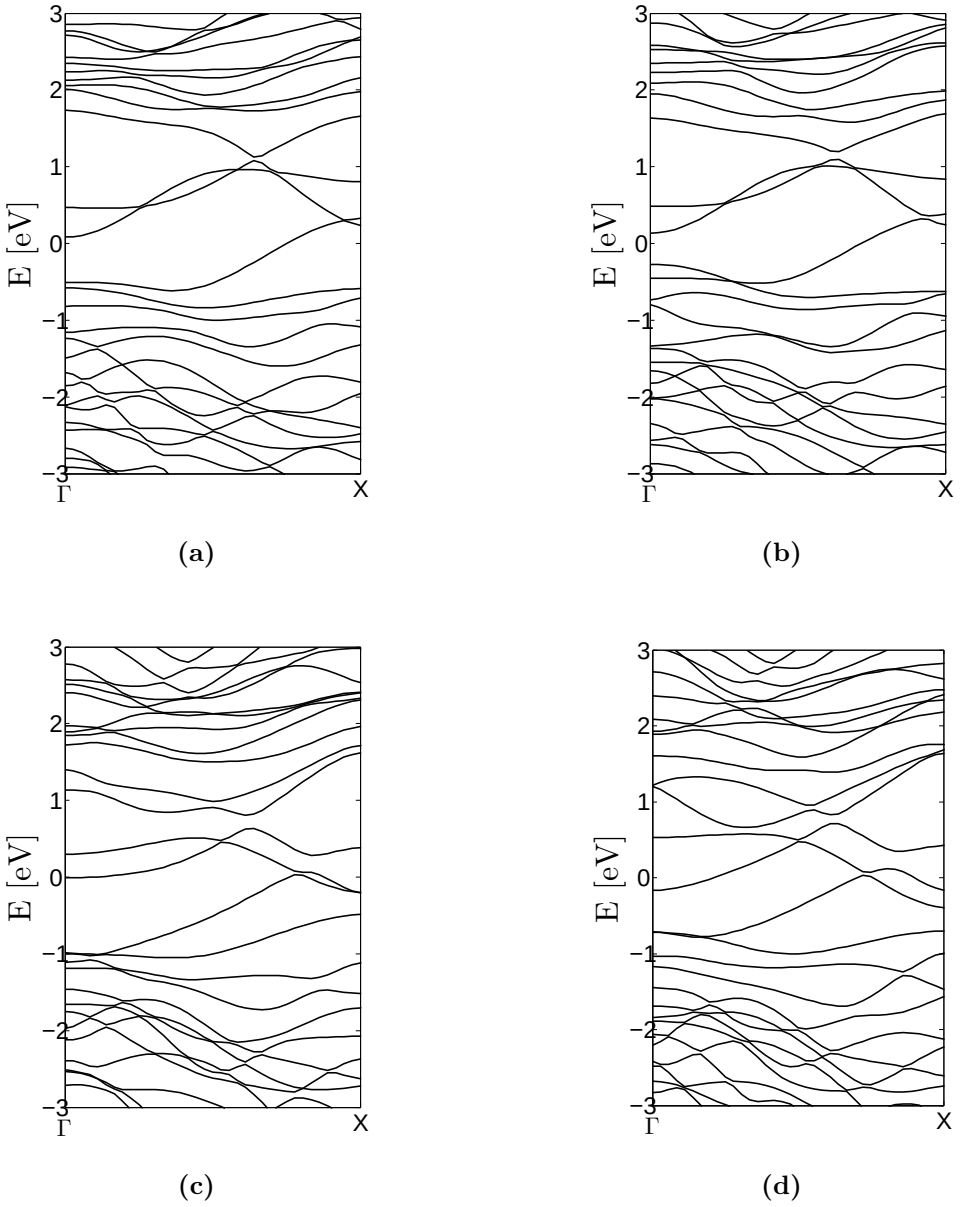

Figure 32 – Band structures of 4-atom wide nanoribbons: (a) $4 - MoS_2$, (b) $4a - MoSSe$, (c) $4b - MoSSe$, (d) $4 - MoSe_2$ NR. The NRs are semimettalic and the band gap slightly decreases for following NRs. Various edge states are apparent in the band gaps and their curvature and crossings change for selenium contribution increasing.

In fact, the evolution of the entire band structure is apparent as the selenium atoms contribution to edges increases. As sulphur atoms are replaced by selenium atoms the energy gap slightly decreases. Also, the curvature of bands changes and some crossings

of the edge states disappear when the selenium atoms are added. All of the nanoribbons appear to be semimetallic despite the changes of the band structure.

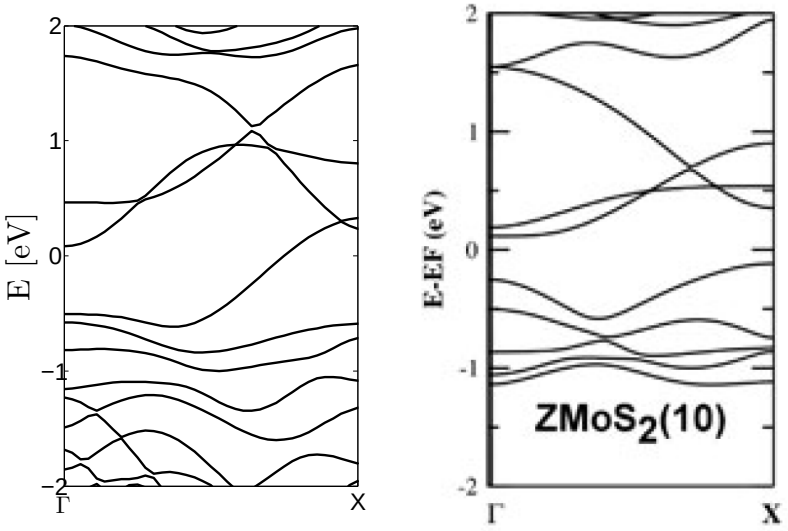

(a) **(b)**

Figure 33 – MoS_2 nanoribbon band structure comparison to known results [93]. The band structure obtained here has been well reproduced. Important differences include several crossings of the states in the gap near Γ and X points.

Band structure of MoS_2 NR is in Fig. 33 in comparison with the results obtained in [93]. The band structure obtained is with good agreement to the reports. However, some differences include existence of some gap states crossings, which may occur due to different exhcange-correlation functional used or the narrow size of the NR.

3.2.4 Magnetic properties.

It is highly important to include analysis of magnetic properties in the studies of TMDC nanostructures. Therefore spin-resolved caluclations have been performed. They allow for determination of spin-dependent electronic densities of NRs and their differences are interpreted as local magnetisation of the crystals.

The projections of magnetisation on the crystal plane for MoS2, MoSSe and MoSe2 ZNRs are presented in Fig. 34. Colors represent its positive and negative values. We observe the highest magnetisation on the unpassivated Mo-edges, which consist of strongly magnetic metal atoms. This magnetisation is diminished when selenium atom contribution to the edges increases. The S-edge magnetisation occuring due to sulphur atoms contribution is not as greatly influenced by addition of selenium atoms.

Basing on the analysis of the color maps we may determine the spin-polarisation of the edges of NRs. It is schematically shown in Fig. 35. It is clear that MoS_2 4-ZNR is ferromagnetic, which has been reported previously [77]. We observe that the MoSSe 4a-ZNR are also ferromagnetic on the edges, while the MoSSe 4b-ZNR and $MoSe_2$ 4-ZNR are antiferromagnetic. Furthermore, the polarisation is the strongest for MoS_2 NR and substitution of selenium atoms reduces it significantly, especially on the Mo-edges.

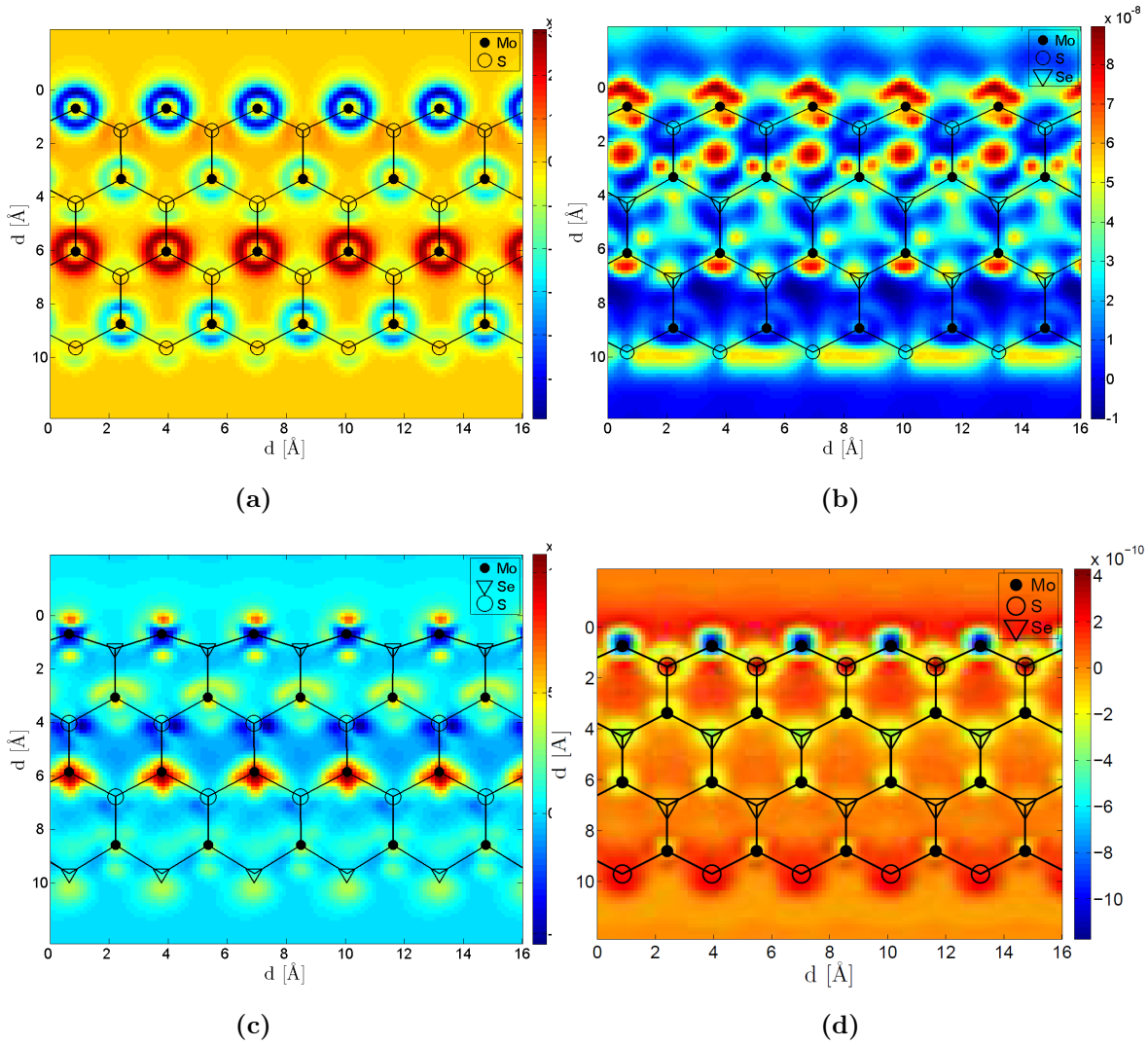

Figure 34 – Local magnetisation projected on the Mo-atom plane for 4-atom wide nanoribbons: (a) $4-MoS_2$, (b) $4a-MoSSe$, (c) $4b-MoSSe$, (d) $4-MoSe_2$ NR. Colors correspond to positive and negative local magnetisations. The largest local magnetisation appears always on the unpassivated Mo-edge. MoS_2 NR has the strongest magnetisations and it decreases for NRs with Se atoms. Ferromagentic edge polarisation is visible in (a-b) and a transition to anti-ferromagnetism can be seen for (c-d). Optimised crystal lattice have been drawn schematically for a clear picture with full (empty) circles representing Mo (S) atoms and triangles standing for Se atoms.

3.2.5 Discussion.

In this section zigzag TMDC nanoribbons were investigated with Abinit package. The DFT calculations have proven to provide information on some properties of MoS_2 ZNR that were impossible to describe with the three-band tight-binding model discussed in the previous section. Band structures have been obtained for MoS_2, which agree well with other reports and the energy bands were calculated for MoSe2 and MoSSe NR as well. Band gaps and edge states apearing in the band gaps have been investigated.

Distortions of the crystal lattices were analysed for ZNRs with 2 and 4 metal atoms in the elementary cell. The largest displacements have been observed for $MoSe_2$ and MoSSe NRs. In particular, unpassivated Mo-edges proved most prone to the distortions.

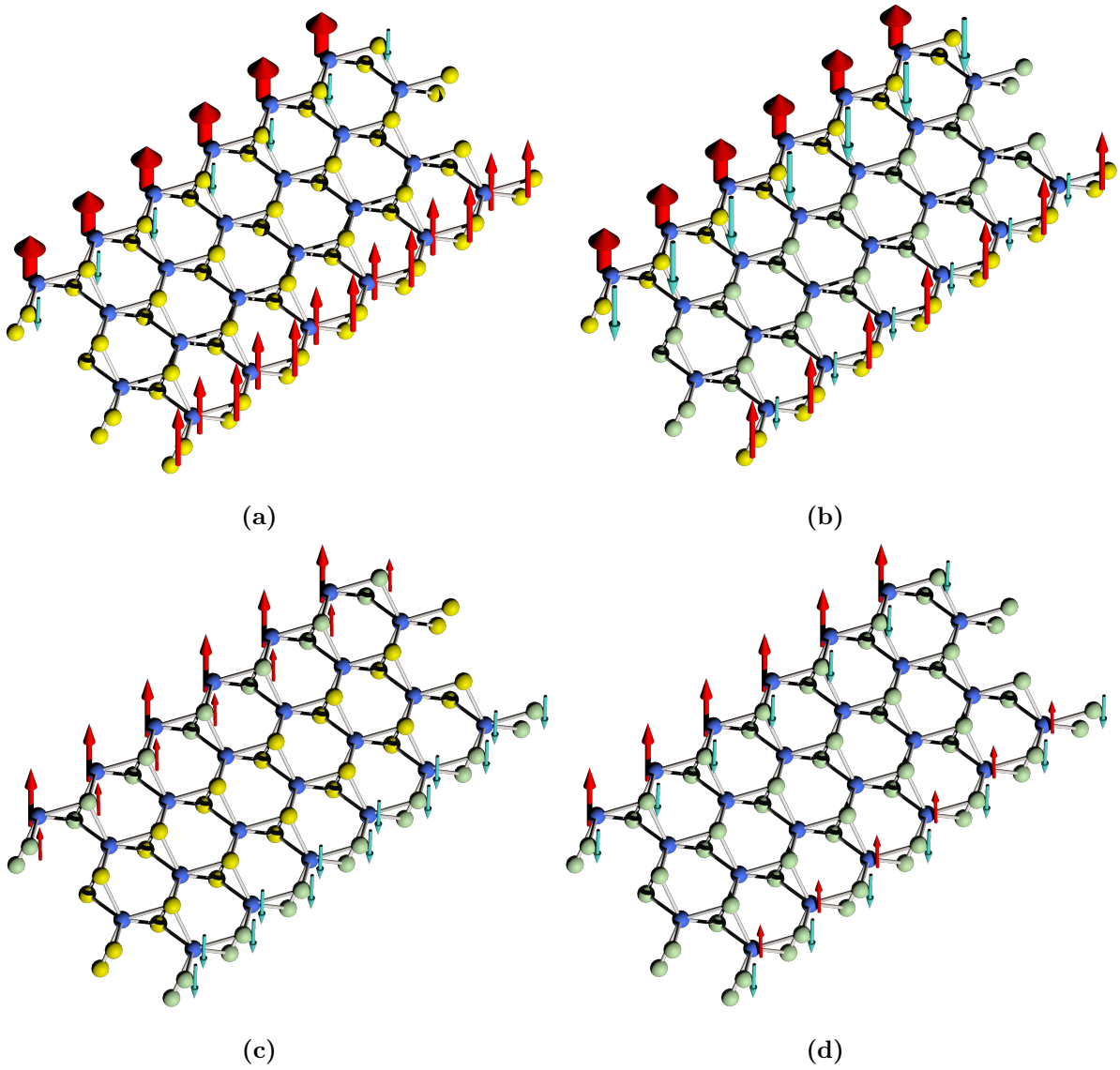

Figure 35 – Edge spin polarisation of 4-Mo-atom wide nanoribbons shown schematically for: (a) $4 - MoS_2$, (b) $4a - MoSSe$, (c) $4b - MoSSe$, (d) $4 - MoSe_2$ NR. Red (blue) arrows stand for positive (negative) magnetisation. Bigger arrows indicate higher values of magnetisation. As Se atoms are added, the magnetisation of Mo-edge decreases and the ferromagnetic spin polarisation of edges changes to antiferromagnetic.

Electronic densities for the optimised structures have been presented. These as well as the low-energy band structures show the importance of the edges in the properties of NRs.

Apart from the electronic properties, the magnetism of the NRs is investigated as well. Spin-dependent electronic densities have been analysed and local magentisation of the NRS has been studied. On this basis the spin-polarisation of the edges of NRs is discussed, which for the ferromagnetic MoS2 NR agrees well with the literature [77]. Imoprtantly, ferro-antiferromagnetic transtion is identified. Its occurence result from the selenium atoms substitution in the NRs' edges which reduces the Mo-edge magnetisation and reverses the polarisation of the edges.

4 Conlusions.

In this work various properties of several types of TMDC nanostructures have been investigated. In section 3.1 the calculations within the three-band approximation to tight-binding model have been performed, following G.B.Liu *et al.* [39]. The object of the study was to obtain the band structures of TMDC monolayers and zigzag-edged nanoribbons. Also, the Hamiltonian for a nanoribbon with armchair edge type has been derived and its band structure has been analysed. For TMDC monolayers, the spin-orbit coupling effect has been included in the calculations. The tight-binding results have been compared to these obtained with DFT methods in Abinit package and with results from literature [39].

It has been concluded that the three-band approximation procudes more accurate results for TMDC monolayers when the contribution from the third nearest neighbours is taken into account. For monolayer TMDC, the reversed spin-split of the bands in the K and K' valleys under spin-orbit coupling effect is reproduced well. This TB model is however not sufficient to describe the properties of MoS_2 nanoribbons as the obtained band structres lack some important low energy states in the band gap. Because this is most likely steming from the fact that the absent states are formed of orbitals neglected in the model (as reported in ref. [39]), the necessity has been stated to develop an extended model inlcuding more orbitals of metal and chalcogen atoms. In view of these conclusions, the model is predicted to give incorrect results in case of any TMDC quantum dots, as the properties of such nanostructures should depend strongly on the edge properties.

Section 3.2 provides the results of DFT calculations in the Abinit package. The parameters of the calculations have been chosen with accordance to literature [108, 109] and have been found as a result of thorough convergence studies. With this method the unpassivated zigzag-edged MoS_2, MoSSe and $MoSe_2$ narrow nanoribbons have been investigated. The geometry of the nanostructures have been optimised and the MoS_2 crystals have been found to distort the least out of the crystals studied. Greatest distortions within nanoribbons have occured at the unpassivated Mo-edge due to unsaturated bonds.

The nanoribbons of optimised geometry have been then analysed in terms of their electronic and magnetic properties. Their band structures have been obtained and analysed, identifying the nanoribbons as semimetallic. Results for the MoS_2 nanoribbon have been compared to literature [93], as this type of nanoribbon has been widely explored [83, 85, 87, 90, 91]. To our knowledge, calculations on MoSSe nanoribbons have not yet been reported. Furthermore, the local magentisation of these nanoribbons have been studied. MoS_2 nanoribbon has been found to have the strongest magentisation, localised mostly on the edges, especially the unpassivated Mo-edge. A transition from ferromagnetic spin polarisation on the edges to antiferromagentically polarised spins has been observed for nanoribbons with increasing selenium-based composition. The selenium atoms have been identified to decrease the magentisation of the Mo-edges and finally induce the anti-ferromagentic spin polarisation for $MoSe_2$ nanoribbon.

From the two methods used in this work, the DFT approach has provided more information about the analysed structures due to the very character of the method, which includes contributions from all atom orbitals. Additionally, the geometries have been optimised, which have affected mostly the edges of the structures, therefore determining to large extent their low-energy properties. Also, as the three-band approximation to tight-binding model does not take chalcogen orbitals into account, any differences between the nanoribbons studied within DFT methods would not have been captured. It is so as they all consist of only one type of metal atom and they differ only by chalcogen atoms. In

effect, the results produced with the three-band tight-binding model would not be correct, as the nanoribbons properties described in DFT methods are significantly different from each other. This motivates again the development of an extended model based on a larger orbital basis, which might then prove more efficient in case of studies of structures bigger than reachable within the unit cell size limit of DFT calculations.

The result obtained in this work provide much insight in the properties of TMDC nanoribbons and other TMDC nanostructures. It is especially valuable in view of recent research in the area of nanodevices developped on the basis on TMDC crystals [65, 66, 69]. Also, since the first in-plane TMDC heterostructures have been reported and their practical advantages have been predicted [63], it is important to emphasize the significance of the results on MoSSe nanoribbons. It is expected that the future studies should focus on larger sizes of similar structures and their more diverse compositions as well as on development of an effective model for these nanostructures.

5 List of figures.

6 References.

[1] K. S. Novoselov, D. Jiang, F. Schedin, T. J. Booth, V. V. Khotkevich, S. V. Morozov, and A. K. Geim, "Two-dimensional atomic crystals," *Proceedings of the National Academy of Sciences of the United States of America*, vol. 102, no. 30, pp. 10451–10453, 2005.

[2] K. S. Novoselov, A. K. Geim, S. V. Morozov, D. Jiang, Y. Zhang, S. V. Dubonos, I. V. Grigorieva, and A. A. Firsov, "Electric field effect in atomically thin carbon films," *Science*, vol. 306, no. 5696, pp. 666–669, 2004.

[3] RadisavljevicB., RadenovicA., BrivioJ., GiacomettiV., and KisA., "Single-layer mos2 transistors," *Nat Nano*, vol. 6, pp. 147–150, Mar 2011.

[4] S. Das, H.-Y. Chen, A. V. Penumatcha, and J. Appenzeller, "High performance multilayer mos2 transistors with scandium contacts," *Nano Letters*, vol. 13, no. 1, pp. 100–105, 2013. PMID: 23240655.

[5] A. S. Mayorov, R. V. Gorbachev, S. V. Morozov, L. Britnell, R. Jalil, L. A. Ponomarenko, P. Blake, K. S. Novoselov, K. Watanabe, T. Taniguchi, and A. K. Geim, "Micrometer-scale ballistic transport in encapsulated graphene at room temperature," *Nano Letters*, vol. 11, no. 6, pp. 2396–2399, 2011. PMID: 21574627.

[6] M. S. Choi, D. Qu, D. Lee, X. Liu, K. Watanabe, T. Taniguchi, and W. J. Yoo, "Lateral mos2 pn junction formed by chemical doping for use in high-performance optoelectronics," *ACS Nano*, vol. 8, no. 9, pp. 9332–9340, 2014. PMID: 25131298.

[7] A. H. Castro Neto, F. Guinea, N. M. R. Peres, K. S. Novoselov, and A. K. Geim, "The electronic properties of graphene," *Rev. Mod. Phys.*, vol. 81, pp. 109–162, Jan 2009.

[8] A. K. Geim, "Graphene: Status and prospects," *Science*, vol. 324, no. 5934, pp. 1530–1534, 2009.

[9] A. Splendiani, L. Sun, Y. Zhang, T. Li, J. Kim, C.-Y. Chim, G. Galli, and F. Wang, "Emerging photoluminescence in monolayer mos2," *Nano Letters*, vol. 10, no. 4, pp. 1271–1275, 2010. PMID: 20229981.

[10] W. Zhao, Z. Ghorannevis, L. Chu, M. Toh, C. Kloc, P.-H. Tan, and G. Eda, "Evolution of electronic structure in atomically thin sheets of ws2 and wse2," *ACS Nano*, vol. 7, no. 1, pp. 791–797, 2013. PMID: 23256505.

[11] A. K. Geim and I. V. Grigorieva, "Van der waals heterostructures," *Nature*, vol. 499, no. 7459, pp. 419–425, 2013.

[12] T. Roy, M. Tosun, J. S. Kang, A. B. Sachid, S. B. Desai, M. Hettick, C. C. Hu, and A. Javey, "Field-effect transistors built from all two-dimensional material components," *ACS Nano*, vol. 8, no. 6, pp. 6259–6264, 2014. PMID: 24779528.

[13] J. Wilson and A. Yoffe, "The transition metal dichalcogenides discussion and interpretation of the observed optical, electrical and structural properties," *Advances in Physics*, vol. 18, no. 73, pp. 193–335, 1969.

[14] A. D. Yoffe, "Layer compounds," *Annual Review of Materials Science*, vol. 3, no. 1, pp. 147–170, 1973.

[15] A. Yoffe, "Low-dimensional systems: quantum size effects and electronic properties of semiconductor microcrystallites (zero-dimensional systems) and some quasi-two-dimensional systems," *Advances in Physics*, vol. 42, no. 2, pp. 173–262, 1993.

[16] C. Stender, E. Greyson, Y. Babayan, and T. Odom, "Patterned mos2 nanostructures over centimeter-square areas," *Advanced Materials*, vol. 17, no. 23, pp. 2837–2841, 2005.

[17] C. L. Stender and T. W. Odom, "Chemical nanofabrication: a general route to surface-patterned and free-standing transition metal chalcogenide nanostructures," *J. Mater. Chem.*, vol. 17, pp. 1866–1869, 2007.

[18] L. Cao, S. Yang, W. Gao, Z. Liu, Y. Gong, L. Ma, G. Shi, S. Lei, Y. Zhang, S. Zhang, R. Vajtai, and P. M. Ajayan, "Direct laser-patterned micro-supercapacitors from paintable mos2 films," *Small*, vol. 9, no. 17, pp. 2905–2910, 2013.

[19] D. Xiao, G.-B. Liu, W. Feng, X. Xu, and W. Yao, "Coupled spin and valley physics in monolayers of mos_2 and other group-vi dichalcogenides," *Phys. Rev. Lett.*, vol. 108, p. 196802, May 2012.

[20] C. Lee, Q. Li, W. Kalb, X.-Z. Liu, H. Berger, R. W. Carpick, and J. Hone, "Frictional characteristics of atomically thin sheets," *Science*, vol. 328, no. 5974, pp. 76–80, 2010.

[21] T. Korn, S. Heydrich, M. Hirmer, J. Schmutzler, and C. Schüller, "Low-temperature photocarrier dynamics in monolayer mos2," *Applied Physics Letters*, vol. 99, no. 10, pp. –, 2011.

[22] A. Splendiani, L. Sun, Y. Zhang, T. Li, J. Kim, C.-Y. Chim, G. Galli, and F. Wang, "Emerging photoluminescence in monolayer mos2," *Nano Letters*, vol. 10, no. 4, pp. 1271–1275, 2010. PMID: 20229981.

[23] J. Zheng, H. Zhang, S. Dong, Y. Liu, C. Tai Nai, H. Suk Shin, H. Young Jeong, B. Liu, and K. Ping Loh, "High yield exfoliation of two-dimensional chalcogenides using sodium naphthalenide," *Nat Commun*, vol. 5, Jan 2014.

[24] A. H. M. A. Wasey, S. Chakrabarty, and G. P. Das, "Substrate induced modulation of electronic, magnetic and chemical properties of mose2 monolayer," *AIP Advances*, vol. 4, no. 4, pp. –, 2014.

[25] F. Wypych and R. Schollhorn, "1t-mos2, a new metallic modification of molybdenum disulfide," *J. Chem. Soc., Chem. Commun.*, pp. 1386–1388, 1992.

[26] Q. H. Wang, K. Kalantar-Zadeh, A. Kis, J. N. Coleman, and M. S. Strano, "Electronics and optoelectronics of two-dimensional transition metal dichalcogenides," *Nat Nano*, vol. 7, pp. 699–712, Nov 2012.

[27] L. F. Mattheiss, "Band structures of transition-metal-dichalcogenide layer compounds," *Phys. Rev. B*, vol. 8, pp. 3719–3740, Oct 1973.

[28] D. Yang, S. J. Sandoval, W. M. R. Divigalpitiya, J. C. Irwin, and R. F. Frindt, "Structure of single-molecular-layer mos_2," *Phys. Rev. B*, vol. 43, pp. 12053–12056, May 1991.

[29] H. Zeng and X. Cui, "An optical spectroscopic study on two-dimensional group-vi transition metal dichalcogenides," *Chem. Soc. Rev.*, vol. 44, pp. 2629–2642, 2015.

[30] K. F. Mak, C. Lee, J. Hone, J. Shan, and T. F. Heinz, "Atomically thin mos_2: A new direct-gap semiconductor," *Phys. Rev. Lett.*, vol. 105, p. 136805, Sep 2010.

[31] G. W. Shim, K. Yoo, S.-B. Seo, J. Shin, D. Y. Jung, I.-S. Kang, C. W. Ahn, B. J. Cho, and S.-Y. Choi, "Large-area single-layer mose2 and its van der waals heterostructures," *ACS Nano*, vol. 8, no. 7, pp. 6655–6662, 2014. PMID: 24987802.

[32] C. M. Orofeo, S. Suzuki, Y. Sekine, and H. Hibino, "Scalable synthesis of layer-controlled ws2 and mos2 sheets by sulfurization of thin metal films," *Applied Physics Letters*, vol. 105, no. 8, pp. –, 2014.

[33] Y. Zhang, T.-R. Chang, B. Zhou, Y.-T. Cui, H. Yan, Z. Liu, F. Schmitt, J. Lee, R. Moore, Y. Chen, H. Lin, H.-T. Jeng, S.-K. Mo, Z. Hussain, A. Bansil, and Z.-X. Shen, "Direct observation of the transition from indirect to direct bandgap in atomically thin epitaxial mose2," *Nat Nano*, vol. 9, pp. 111–115, Feb 2014. Letter.

[34] K. F. Mak, C. Lee, J. Hone, J. Shan, and T. F. Heinz, "Atomically thin mos_2: A new direct-gap semiconductor," *Phys. Rev. Lett.*, vol. 105, p. 136805, Sep 2010.

[35] A. Splendiani, L. Sun, Y. Zhang, T. Li, J. Kim, C.-Y. Chim, G. Galli, and F. Wang, "Emerging photoluminescence in monolayer mos2," *Nano Letters*, vol. 10, no. 4, pp. 1271–1275, 2010. PMID: 20229981.

[36] V. Podzorov, M. E. Gershenson, C. Kloc, R. Zeis, and E. Bucher, "High-mobility field-effect transistors based on transition metal dichalcogenides," *Applied Physics Letters*, vol. 84, no. 17, pp. 3301–3303, 2004.

[37] R. Kappera, D. Voiry, S. E. Yalcin, B. Branch, G. Gupta, A. D. Mohite, and M. Chhowalla, "Phase-engineered low-resistance contacts for ultrathin mos2 transistors," *Nat Mater*, vol. 13, pp. 1128–1134, Dec 2014. Article.

[38] S. Das, H.-Y. Chen, A. V. Penumatcha, and J. Appenzeller, "High performance multilayer mos2 transistors with scandium contacts," *Nano Letters*, vol. 13, no. 1, pp. 100–105, 2013. PMID: 23240655.

[39] G.-B. Liu, W.-Y. Shan, Y. Yao, W. Yao, and D. Xiao, "Three-band tight-binding model for monolayers of group-vib transition metal dichalcogenides," *Phys. Rev. B*, vol. 88, p. 085433, Aug 2013.

[40] D. Xiao, W. Yao, and Q. Niu, "Valley-contrasting physics in graphene: Magnetic moment and topological transport," *Phys. Rev. Lett.*, vol. 99, p. 236809, Dec 2007.

[41] W. Yao, D. Xiao, and Q. Niu, "Valley-dependent optoelectronics from inversion symmetry breaking," *Phys. Rev. B*, vol. 77, p. 235406, Jun 2008.

[42] O. Gunawan, Y. P. Shkolnikov, K. Vakili, T. Gokmen, E. P. De Poortere, and M. Shayegan, "Valley susceptibility of an interacting two-dimensional electron system," *Phys. Rev. Lett.*, vol. 97, p. 186404, Nov 2006.

[43] E. S. Kadantsev and P. Hawrylak, "Electronic structure of a single mos2 monolayer," *Solid State Communications*, vol. 152, no. 10, pp. 909 – 913, 2012.

[44] T. Cao, G. Wang, W. Han, H. Ye, C. Zhu, J. Shi, Q. Niu, P. Tan, E. Wang, B. Liu, and J. Feng, "Valley-selective circular dichroism of monolayer molybdenum disulphide," *Nat Commun*, vol. 3, p. 887, Jun 2012.

[45] H. Zeng, J. Dai, W. Yao, D. Xiao, and X. Cui, "Valley polarization in mos2 monolayers by optical pumping," *Nat Nano*, vol. 7, pp. 490–493, Aug 2012.

[46] A. M. Jones, H. Yu, N. J. Ghimire, S. Wu, G. Aivazian, J. S. Ross, B. Zhao, J. Yan, D. G. Mandrus, D. Xiao, W. Yao, and X. Xu, "Optical generation of excitonic valley coherence in monolayer wse2," *Nat Nano*, vol. 8, pp. 634–638, Sep 2013. Letter.

[47] S. Wu, J. S. Ross, G.-B. Liu, G. Aivazian, A. Jones, Z. Fei, W. Zhu, D. Xiao, W. Yao, D. Cobden, and X. Xu, "Electrical tuning of valley magnetic moment through symmetry control in bilayer mos2," *Nat Phys*, vol. 9, pp. 149–153, Mar 2013.

[48] X. Xu, W. Yao, D. Xiao, and T. F. Heinz, "Spin and pseudospins in layered transition metal dichalcogenides," *Nat Phys*, vol. 10, pp. 343–350, May 2014. Review.

[49] T. Cai, S. A. Yang, X. Li, F. Zhang, J. Shi, W. Yao, and Q. Niu, "Magnetic control of the valley degree of freedom of massive dirac fermions with application to transition metal dichalcogenides," *Phys. Rev. B*, vol. 88, p. 115140, Sep 2013.

[50] W. Feng, Y. Yao, W. Zhu, J. Zhou, W. Yao, and D. Xiao, "Intrinsic spin hall effect in monolayers of group-vi dichalcogenides: A first-principles study," *Phys. Rev. B*, vol. 86, p. 165108, Oct 2012.

[51] H. Rostami and R. Asgari, "Valley zeeman effect and spin-valley polarized conductance in monolayer mos_2 in a perpendicular magnetic field," *Phys. Rev. B*, vol. 91, p. 075433, Feb 2015.

[52] D. MacNeill, C. Heikes, K. F. Mak, Z. Anderson, A. Kormányos, V. Zólyomi, J. Park, and D. C. Ralph, "Breaking of valley degeneracy by magnetic field in monolayer $mose_2$," *Phys. Rev. Lett.*, vol. 114, p. 037401, Jan 2015.

[53] R.-L. Chu, X. Li, S. Wu, Q. Niu, W. Yao, X. Xu, and C. Zhang, "Valley-splitting and valley-dependent inter-landau-level optical transitions in monolayer mos_2 quantum hall systems," *Phys. Rev. B*, vol. 90, p. 045427, Jul 2014.

[54] F. Rose, M. O. Goerbig, and F. Piéchon, "Spin- and valley-dependent magneto-optical properties of mos_2," *Phys. Rev. B*, vol. 88, p. 125438, Sep 2013.

[55] X. Qian, J. Liu, L. Fu, and J. Li, "Quantum spin hall effect in two-dimensional transition metal dichalcogenides," *Science*, 2014.

[56] N. F. Q. Yuan, K. F. Mak, and K. T. Law, "Possible topological superconducting phases of mos_2," *Phys. Rev. Lett.*, vol. 113, p. 097001, Aug 2014.

[57] G.-B. Liu, H. Pang, Y. Yao, and W. Yao, "Intervalley coupling by quantum dot confinement potentials in monolayer transition metal dichalcogenides," *New Journal of Physics*, vol. 16, no. 10, p. 105011, 2014.

[58] J. V. Lauritsen, J. Kibsgaard, S. Helveg, H. Topsoe, B. S. Clausen, E. Laegsgaard, and F. Besenbacher, "Size-dependent structure of mos2 nanocrystals," *Nat Nano*, vol. 2, pp. 53–58, Jan 2007.

[59] Z. Wang, H. Li, Z. Liu, Z. Shi, J. Lu, K. Suenaga, S.-K. Joung, T. Okazaki, Z. Gu, J. Zhou, Z. Gao, G. Li, S. Sanvito, E. Wang, and S. Iijima, "Mixed low-dimensional nanomaterial: 2d ultranarrow mos2 inorganic nanoribbons encapsulated in quasi-1d carbon nanotubes," *Journal of the American Chemical Society*, vol. 132, no. 39, pp. 13840–13847, 2010. PMID: 20828123.

[60] J. V. Lauritsen, J. Kibsgaard, S. Helveg, H. Topsoe, B. S. Clausen, E. Laegsgaard, and F. Besenbacher, "Size-dependent structure of mos2 nanocrystals," *Nat Nano*, vol. 2, pp. 53–58, Jan 2007.

[61] A. Tuxen, J. Kibsgaard, H. Gobel, E. Lagsgaard, H. Topsoe, J. V. Lauritsen, and F. Besenbacher, "Size threshold in the dibenzothiophene adsorption on mos2 nanoclusters," *ACS Nano*, vol. 4, no. 8, pp. 4677–4682, 2010. PMID: 20604573.

[62] H. Füchtbauer, A. Tuxen, Z. Li, H. Topsoe, J. Lauritsen, and F. Besenbacher, "Morphology and atomic-scale structure of mos2 nanoclusters synthesized with different sulfiding agents," *Topics in Catalysis*, vol. 57, no. 1-4, pp. 207–214, 2014.

[63] C. Huang, S. Wu, A. M. Sanchez, J. J. P. Peters, R. Beanland, J. S. Ross, P. Rivera, W. Yao, D. H. Cobden, and X. Xu, "Lateral heterojunctions within monolayer mose2-wse2 semiconductors," *Nat Mater*, vol. 13, pp. 1096–1101, Dec 2014. Letter.

[64] Y. Gong, J. Lin, X. Wang, G. Shi, S. Lei, Z. Lin, X. Zou, G. Ye, R. Vajtai, B. I. Yakobson, H. Terrones, M. Terrones, B. Tay, J. Lou, S. T. Pantelides, Z. Liu, W. Zhou, and P. M. Ajayan, "Vertical and in-plane heterostructures from ws2/mos2 monolayers," *Nat Mater*, vol. 13, pp. 1135–1142, Dec 2014. Article.

[65] S. Ghatak, A. N. Pal, and A. Ghosh, "Nature of electronic states in atomically thin mos2 field-effect transistors," *ACS Nano*, vol. 5, no. 10, pp. 7707–7712, 2011. PMID: 21902203.

[66] J. Qi, Y.-W. Lan, A. Z. Stieg, J.-H. Chen, Y.-L. Zhong, L.-J. Li, C.-D. Chen, Y. Zhang, and K. L. Wang, "Piezoelectric effect in chemical vapour deposition-grown atomic-monolayer triangular molybdenum disulfide piezotronics," *Nat Commun*, vol. 6, Jun 2015. Article.

[67] J. Na, M.-K. Joo, M. Shin, J. Huh, J.-S. Kim, M. Piao, J.-E. Jin, H.-K. Jang, H. J. Choi, J. H. Shim, and G.-T. Kim, "Low-frequency noise in multilayer mos2 field-effect transistors: the effect of high-k passivation," *Nanoscale*, vol. 6, pp. 433–441, 2014.

[68] W. Wu, L. Wang, Y. Li, F. Zhang, L. Lin, S. Niu, D. Chenet, X. Zhang, Y. Hao, T. F. Heinz, J. Hone, and Z. L. Wang, "Piezoelectricity of single-atomic-layer mos2 for energy conversion and piezotronics," *Nature*, vol. 514, pp. 470–474, Oct 2014. Letter.

[69] S. P. Giblin, M. Kataoka, J. D. Fletcher, P. See, T. J. B. M. Janssen, J. P. Griffiths, G. A. C. Jones, I. Farrer, and D. A. Ritchie, "Towards a quantum representation of the ampere using single electron pumps," *Nat Commun*, vol. 3, p. 930, Jul 2012.

[70] K. L. McBride and J. D. Head, "Dft investigation of mos2 nanoclusters used as desulfurization catalysts," *International Journal of Quantum Chemistry*, vol. 109, no. 15, pp. 3570–3582, 2009.

[71] J. Lin, O. Cretu, W. Zhou, K. Suenaga, D. Prasai, K. I. Bolotin, N. T. Cuong, M. Otani, S. Okada, A. R. Lupini, J.-C. Idrobo, D. Caudel, A. Burger, N. J. Ghimire, J. Yan, D. G. Mandrus, S. J. Pennycook, and S. T. Pantelides, "Flexible metallic nanowires with self-adaptive contacts to semiconducting transition-metal dichalcogenide monolayers," *Nat Nano*, vol. 9, pp. 436–442, Jun 2014. Letter.

[72] R. Tenne, L. Margulis, M. Genut, and G. Hodes, "Polyhedral and cylindrical structures of tungsten disulphide," *Nature*, vol. 360, pp. 444–446, Dec 1992.

[73] F. Ding, W. Zhao, w. Duan, and Y. Li, "Ultra-stable small diameter hybrid transition metal dichalcogenide nanotubes x-m-y (x, y = s, se, te; m = mo, w, nb, ta): A computational study," *Nanoscale*, pp. –, 2015.

[74] L. Peng, K. Yao, S. Zhu, Y. Ni, F. Zu, S. Wang, B. Guo, and Y. Tian, "Spin transport properties of partially edge-hydrogenated mos2 nanoribbon heterostructure," *Journal of Applied Physics*, vol. 115, no. 22, pp. –, 2014.

[75] G. Seifert, J. Tamuliene, and S. Gemming, "Mons2n+x clusters magic numbers and platelets," *Computational Materials Science*, vol. 35, no. 3, pp. 316 – 320, 2006. Proceedings of the 4th International Conference on the Theory of Atomic and Molecular Clusters (TAMC-IV) The 4th International Conference on the Theory of Atomic and Molecular Clusters.

[76] Y. Zhou, P. Yang, H. Zu, F. Gao, and X. Zu, "Electronic structures and magnetic properties of mos2 nanostructures: atomic defects, nanoholes, nanodots and antidots," *Phys. Chem. Chem. Phys.*, vol. 15, pp. 10385–10394, 2013.

[77] H. Pan and Y.-W. Zhang, "Edge-dependent structural, electronic and magnetic properties of mos2 nanoribbons," *J. Mater. Chem.*, vol. 22, pp. 7280–7290, 2012.

[78] F. López-Urías, A. L. Elías, N. Perea-López, H. R. Gutiérrez, M. Terrones, and H. Terrones, "Electronic, magnetic, optical, and edge-reactivity properties of semiconducting and metallic ws 2 nanoribbons," *2D Materials*, vol. 2, no. 1, p. 015002, 2015.

[79] K. Kośmider, J. W. González, and J. Fernández-Rossier, "Large spin splitting in the conduction band of transition metal dichalcogenide monolayers," *Phys. Rev. B*, vol. 88, p. 245436, Dec 2013.

[80] F. Zahid, L. Liu, Y. Zhu, J. Wang, and H. Guo, "A generic tight-binding model for monolayer, bilayer and bulk mos2," *AIP Advances*, vol. 3, no. 5, pp. –, 2013.

[81] H. Rostami, A. G. Moghaddam, and R. Asgari, "Effective lattice hamiltonian for monolayer mos_2: Tailoring electronic structure with perpendicular electric and magnetic fields," *Phys. Rev. B*, vol. 88, p. 085440, Aug 2013.

[82] E. Cappelluti, R. Roldán, J. A. Silva-Guillén, P. Ordejón, and F. Guinea, "Tight-binding model and direct-gap/indirect-gap transition in single-layer and multilayer mos_2," *Phys. Rev. B*, vol. 88, p. 075409, Aug 2013.

[83] K. Dolui, C. D. Pemmaraju, and S. Sanvito, "Electric field effects on armchair mos2 nanoribbons," *ACS Nano*, vol. 6, no. 6, pp. 4823–4834, 2012. PMID: 22546015.

[84] L. Kou, C. Tang, Y. Zhang, T. Heine, C. Chen, and T. Frauenheim, "Tuning magnetism and electronic phase transitions by strain and electric field in zigzag mos2 nanoribbons," *The Journal of Physical Chemistry Letters*, vol. 3, no. 20, pp. 2934–2941, 2012.

[85] A. Sengupta and S. Mahapatra, "Negative differential resistance and effect of defects and deformations in mos2 armchair nanoribbon metal-oxide-semiconductor field effect transistor," *Journal of Applied Physics*, vol. 114, no. 19, pp. –, 2013.

[86] S. Yang, D. Li, T. Zhang, Z. Tao, and J. Chen, "First-principles study of zigzag mos2 nanoribbon as a promising cathode material for rechargeable mg batteries," *The Journal of Physical Chemistry C*, vol. 116, no. 1, pp. 1307–1312, 2012.

[87] H. Pan and Y.-W. Zhang, "Tuning the electronic and magnetic properties of mos2 nanoribbons by strain engineering," *The Journal of Physical Chemistry C*, vol. 116, no. 21, pp. 11752–11757, 2012.

[88] Q. Yue, S. Chang, J. Kang, X. Zhang, Z. Shao, S. Qin, and J. Li, "Bandgap tuning in armchair mos 2 nanoribbon," *Journal of Physics: Condensed Matter*, vol. 24, no. 33, p. 335501, 2012.

[89] Y. Li, Z. Zhou, S. Zhang, and Z. Chen, "Mos2 nanoribbons: High stability and unusual electronic and magnetic properties," *Journal of the American Chemical Society*, vol. 130, no. 49, pp. 16739–16744, 2008. PMID: 19007118.

[90] A. R. Botello-Méndez, F. López-Urías, M. Terrones, and H. Terrones, "Metallic and ferromagnetic edges in molybdenum disulfide nanoribbons," *Nanotechnology*, vol. 20, no. 32, p. 325703, 2009.

[91] Z. Qi, P. Cao, and H. S. Park, "Density functional theory calculation of edge stresses in monolayer mos2," *Journal of Applied Physics*, vol. 114, no. 16, pp. –, 2013.

[92] B. Ghosh and N. Kishor, "An ab initio study of strained two-dimensional mose 2," *Journal of Semiconductors*, vol. 36, no. 4, p. 043001, 2015.

[93] E. Erdogan, I. Popov, A. Enyashin, and G. Seifert, "Transport properties of mos2 nanoribbons: edge priority," *The European Physical Journal B*, vol. 85, no. 1, 2012.

[94] Y. Li, S. Tongay, Q. Yue, J. Kang, J. Wu, and J. Li, "Metal to semiconductor transition in metallic transition metal dichalcogenides," *Journal of Applied Physics*, vol. 114, no. 17, pp. –, 2013.

[95] M. Sagynbaeva, P. Panigrahi, L. Yunguo, M. Ramzan, and R. Ahuja, "Tweaking the magnetism of mos 2 nanoribbon with hydrogen and carbon passivation," *Nanotechnology*, vol. 25, no. 16, p. 165703, 2014.

[96] S. Tongay, S. S. Varnoosfaderani, B. R. Appleton, J. Wu, and A. F. Hebard, "Magnetic properties of mos2: Existence of ferromagnetism," *Applied Physics Letters*, vol. 101, no. 12, pp. –, 2012.

[97] R. Zhang, Y. Li, J. Qi, and D. Gao, "Ferromagnetism in ultrathin mos2 nanosheets: from amorphous to crystalline," *Nanoscale Research Letters*, vol. 9, no. 1, p. 586, 2014.

[98] R. Shidpour and M. Manteghian, "A density functional study of strong local magnetism creation on mos2 nanoribbon by sulfur vacancy," *Nanoscale*, vol. 2, pp. 1429–1435, 2010.

[99] L. Xin-Mei, L. Meng-Qiu, C. Li-Ling, X. Jin, and X. Hui, "Electronic and transport properties of v-shaped defect zigzag mos 2 nanoribbons," *Chinese Physics B*, vol. 23, no. 4, p. 047307, 2014.

[100] F. Ouyang, Z. Yang, X. Ni, N. Wu, Y. Chen, and X. Xiong, "Hydrogenation-induced edge magnetization in armchair mos2 nanoribbon and electric field effects," *Applied Physics Letters*, vol. 104, no. 7, pp. –, 2014.

[101] T. Hu, J. Zhou, J. Dong, and Y. Kawazoe, "Electronic and magnetic properties of armchair mos2 nanoribbons under both external strain and electric field, studied by first principles calculations," *Journal of Applied Physics*, vol. 116, no. 6, pp. –, 2014.

[102] K. Kośmider and J. Fernández-Rossier, "Electronic properties of the mos_2-ws_2 heterojunction," *Phys. Rev. B*, vol. 87, p. 075451, Feb 2013.

[103] P. Yu and M. Cardona, "Electronic band structures," in *Fundamentals of Semiconductors*, Graduate Texts in Physics, pp. 17–105, Springer Berlin Heidelberg, 1996.

[104] H. Pan and Y.-W. Zhang, "Tuning the electronic and magnetic properties of mos2 nanoribbons by strain engineering," *The Journal of Physical Chemistry C*, vol. 116, no. 21, pp. 11752–11757, 2012.

[105] L. Piela, *Idee chemii kwantowej*. Warszawa: Wydawnictwo Naukowe PWN, 2005.

[106] C. Hartwigsen, S. Goedecker, and J. Hutter, "Relativistic separable dual-space gaussian pseudopotentials from h to rn," *Phys. Rev. B*, vol. 58, pp. 3641–3662, Aug 1998.

[107] P. E. Blöchl, "Projector augmented-wave method," *Phys. Rev. B*, vol. 50, pp. 17953–17979, Dec 1994.

[108] Y. Li, S. Tongay, Q. Yue, J. Kang, J. Wu, and J. Li, "Metal to semiconductor transition in metallic transition metal dichalcogenides," *Journal of Applied Physics*, vol. 114, no. 17, pp. –, 2013.

[109] Q. Yue, S. Chang, J. Kang, X. Zhang, Z. Shao, S. Qin, and J. Li, "Bandgap tuning in armchair mos 2 nanoribbon," *Journal of Physics: Condensed Matter*, vol. 24, no. 33, p. 335501, 2012.

[110] H. J. Monkhorst and J. D. Pack, "Special points for brillouin-zone integrations," *Phys. Rev. B*, vol. 13, pp. 5188–5192, Jun 1976.

[111] H. Zeng and X. Cui, "An optical spectroscopic study on two-dimensional group-vi transition metal dichalcogenides," *Chem. Soc. Rev.*, vol. 44, pp. 2629–2642, 2015.

[112] H. Terrones, F. López-Urías, and M. Terrones, "Novel hetero-layered materials with tunable direct band gaps by sandwiching different metal disulfides and diselenides," *Sci. Rep.*, vol. 3, Mar 2013.